SGP-TR-210

Development of a Downhole Technique for Measuring Enthalpy in Geothermal Wells

Xuhua Gao

June 2017

Financial support was provided by
the Department of Energy Resources Engineering,
Stanford University

Stanford Geothermal Program
Interdisciplinary Research in
Engineering and Earth Sciences
STANFORD UNIVERSITY
Stanford, California

Abstract

A downhole technique for measuring enthalpy in two-phase geothermal wells was investigated in this study. It was proposed that the flowing enthalpy in the downhole could be determined by measuring chloride concentration of the geothermal liquid. Chloride always stays in the liquid phase and becomes more concentrated as the geothermal fluid ascends to the surface and boils, and the change of chloride concentration could be utilized to calculate the change of flowing steam fraction and the enthalpy. Analytical models to implement this idea were established, and the calculation procedures are elaborated with detailed flow diagrams and examples. The analytical model for enthalpy calculation with single feed zone involves mass balance of chloride and total mass balance of liquid and steam. Enthalpy calculations with multiple feed zones are more complicated, and the analytical model for multiple feed zones involves energy balance and an assumption that the chloride concentration of the liquid from the feed zone is measurable. The measurement of chloride concentration was realized by a downhole tool developed by Sandia National Laboratories. Experimental studies were conducted to calibrate the tool and test the performance of the tool in two-phase flow. The calibration of the tool provided a linear relationship between the voltage and the logarithm (base 10) of the chloride concentration. The chloride concentration measured in two-phase flow is slightly lower than that measured in liquid flow, but the relative error is acceptable. Based on the range of relative error provided by the experiment, the range of relative error in enthalpy estimation was calculated. In the experiment, liquid from the feed zone with high chloride concentration was injected into the wellbore through a sidewall injection port. Chloride concentration distribution in the mixing zone was measured using the downhole tool. The highest chloride concentration was obtained when the tool is placed against the wall of the wellbore, and the highest measurement reached the chloride concentration of the injected liquid. The mixing zone was visualized in a dye tracer experiment, and videos were taken to record the mixing process. Computer vision methods were applied to convert the original videos into streams of binary images. Distributions of the mixing zone and the penetration distance were analyzed using the binary images. The mixing process was also visualized by numerical simulation using ANSYS Fluent, which is a commercial computational fluid dynamics software tool. Two types of feed zone inlets were considered in the simulation model, including injection port and horizontal fracture. Simulation results based on the first type of inlet were compared to the experimental results, and similar mixing zone shapes were found. Simulation results based on the second type of inlet visualized the mixing process of the fluid from the fracture with the fluid in the well. An annular mixing zone was observed with the second type of feed zone inlet.

These analytical, experimental and numerical studies of the downhole technique demonstrated the feasibility of determining downhole enthalpy in two-phase flow from multiple feed zones based on chloride concentration measurement.

Acknowledgments

I would like to thank Sandia National Laboratories for the financial support to this work. I am grateful to the Department of Energy Resources Engineering for supporting my master's study.

I am grateful to my advisor, Prof. Roland N. Horne, who has been guiding and supporting me with great patience. His expert suggestions illuminated my research and really inspired me. I would like to say thanks to Dr. Kewen Li for his kindness, help and his valuable advice regarding the experiments. I would like to thank Maytham I. Al Ismail, Yuran Zhang, Renfeng Jiang and Anna Suzuki for offering help and instruction in the laboratory. I am grateful to all my colleagues at the Stanford Geothermal Group for their time and insight. I really appreciate the weekly group meeting with Jack Norbeck, Morgan Ames, Anna Suzuki, Carla Co, Yuran Zhang, Halldora Gudmundsdottir, Yang Wong, Renfeng Zhang, and Ayaka Abe.

Special thanks to Grzegorz Cieslewski, Avery Cashion, Sasha Egan, William Corbin and Ryan Hess from Sandia National Laboratories for their kind support to this work, their efforts in developing the downhole tool, and their generosity in lending me the tool for the experiments.

I would like to thank Wenhao Chen and Qing Yin from the Department of Civil and Environmental Engineering for their instruction on the software ANSYS Fluent. I am grateful to Wenhao Chen for his patience and time.

I am deeply grateful to my parents Hongbo Gao and Shuangyan Lv and my partner Jingfan Wang, whose support and love encourage me along the way. I want to thank all the family members and friends for all the happiness and joy.

Contents

List of Tables

List of Figures

Chapter 1

1. Introduction

1.1. Motivation

The heat energy extracted from geothermal reservoirs is carried by the geothermal fluid, and the amount of extractable energy from a geothermal reservoir is determined by the thermal energy contained in the geothermal fluid, which is measured in terms of the enthalpy. The enthalpy of the geothermal fluid is defined as the energy content per unit mass of the fluid, and a common unit for enthalpy is kJ/kg. The enthalpy of single-phase geothermal fluid is simply the enthalpy of steam or liquid water, which can be calculated directly from temperature or pressure, while for two-phase geothermal fluid, the total enthalpy is the enthalpy of the mixture of steam and liquid water. Measurement of enthalpy in two-phase geothermal wells is an important monitoring task. The total amount of available energy is determined by the total enthalpy of the two-phase mixture and the mass flow rate, so measurement of enthalpy and mass flow rate are routine procedures for geothermal field analysis.

Currently enthalpy measurement is much easier to conduct at the surface, thus surface measurement more commonly used. However, surface enthalpy cannot reflect real reservoir conditions accurately due to the heat loss along the wellbore. This is especially true during the drilling and completion stages. The well has been cooled substantially during drilling so the actual downhole enthalpy is unknown. Downhole enthalpy data could help us better understand reservoir performance and predict future performance, and they would be useful for reservoir modeling and validation of wellbore simulation. Therefore, downhole enthalpy determination is of high value from both operational perspective and economic perspective.

However, determining downhole enthalpy is not easy, especially for two-phase flow. Boiling of geothermal fluids along the wellbore makes it even more complicated. Measuring downhole pressure or temperature is necessary but insufficient for two-phase enthalpy determination, and the key is to determine the flowing steam fraction of the two-phase mixture.

Note that flowing enthalpy is different from in-place or static enthalpy. Flowing enthalpy is based on specific flow rate of steam and water while static enthalpy is based on the mass fraction of steam and water in a certain volume (Brennen 2005). The definition of static enthalpy and flowing enthalpy are expressed in Equation (1-1) and Equation (1-2) respectively. The definition of flowing steam fraction is expressed in Equation (1-3).

$$h_{static} = x_s h_v + (1 - x_s) h_w \tag{1-1}$$

$$h_{flowing} = x_f h_v + (1 - x_f) h_w \tag{1-2}$$

$$x_f = \frac{W_v}{W_v + W_w} \tag{1-3}$$

where

- h_{static} is static enthalpy, kJ/kg
- x_s is static steam fraction by mass
- $h_{flowing}$ is flowing enthalpy, kJ/kg
- x_f is flowing steam fraction
- W_v is steam mass flow rate kg/s
- W_w is water mass flow rate kg/s

h_v and h_w can be determined from pressure or temperature. It is flowing enthalpy that we are trying to measure in the wellbore.

The major difference between the static enthalpy and flowing enthalpy is caused by the difference between the velocity of the gas phase and the velocity of the liquid phase, typically the velocity of the gas phase is larger than the velocity of the liquid phase. The ratio of the gas velocity to the liquid velocity is called "slip ratio" (Moody, 1965), which is an important parameter in calculating two-phase flow properties. Higher slip ratio indicates larger difference between gas velocity and liquid velocity and larger difference between static enthalpy and flowing enthalpy.

Several methods have been developed for calculation or measurement of downhole enthalpy. Some researchers proposed that steam-phase velocity, gas-phase velocity and void fraction could be measured to calculate flowing enthalpy (Spielman, 2003; Juliusson, 2006; Atalay, 2008), as illustrated in Equation (1-4).

$$h_{flowing} = \frac{u_l (1-\alpha) \rho_l h_l + u_g \alpha \rho_g h_g}{u_l (1-\alpha) \rho_l + u_g \alpha \rho_g} \tag{1-4}$$

where

- u_l is liquid-phase velocity, m/s
- u_g is gas-phase velocity, m/s
- ρ_l is density of the liquid phase, kg/m^3
- ρ_g is density of the gas phase, kg/m^3
- α is void fraction

Void fraction represents the fraction of cross-sectional area that is occupied by the gas phase in the pipe. One way to measure the velocity of the gas phase and the void fraction is to use a fiber optic (Atalay 2008), which is an optical sensor that can be used for phase detection. With fiber optics, gas-phase velocity can be determined directly by measuring the time difference for a bubble to pass the two sensors. Void fraction can be measured by a time-averaging procedure. Another approach to measure gas velocity and void

fraction was proposed by Spielman (2003) and Juliusson (2006), who showed that resistivity measurement with sufficient resolution could be applied to detect gas bubbles in two-phase flow. The sharp change of resistivity is an indication of the presence of gas phase, so that the gas velocity can be inferred from the resistivity profile along with the time. The two methods share a similar principle that the detection of gas bubbles can help determining gas velocity and void fraction. Although fiber optics and high-resolution electrodes are efficient for downhole enthalpy measurement in bubble flow, but they are ineffective with other flow types, like annular flow and slug flow. In addition, fiber optic sensors or electrodes can only measure the gas-phase velocity and the liquid-phase velocity has to be measured with other equipment at the same time. Khasani et al. (2010) showed that the analysis of sound frequency waves could provide information on steam and water flow rate, but the method must be calibrated with many wells using standard methods of flow rate measurement in practical application.

Another approach to determine downhole enthalpy is the tracer dilution technique. This method was initially tested on a field-wide basis at the Coso geothermal field in California (Hirtz et al. 1995). Conventional tracer dilution techniques require precisely metered injection of liquid and vapor phase tracers (Hirtz et al. 1993). Mass flowrate of each phase can be calculated based on the injection rate of each tracer at the injection well and the concentration of each tracer measured concurrently with tracer injection at the production well. Tracers that have been considered for use include inorganic ions (CaF_2, LiCl, etc.) as liquid-phase tracers and volatile organic gases (ethane, alcohol, etc.) as gas-phase tracers. For vapor-phase tracers, it is necessary to consider the correction for the tracer gas dissolved in the liquid phase, which is a major drawback of the vapor tracer dilution technique (Lovelock, 2001).

1.2. Purpose of Study

Chloride is an important component in the geothermal fluid and can be utilized as an indicator of various fluid properties (Gendenjamts, 2003). Hess et al. (2015) designed a ruggedized downhole tool to measure real-time concentration of ionic tracers in geothermal reservoirs. Cieslewski et al. (2016) proposed a wireline tool to measure real-time ionic concentration using an electrochemical sensor. Corbin et al. (2017) illustrated a downhole tool to measure real-time chloride concentration in the geothermal fluid. Inspired by the downhole tool introduced by Corbin et al., we proposed that change of chloride concentration along the wellbore could be utilized to calculate downhole enthalpy. It is known that some solutes in the fluid (eg. Cl) always stay in the liquid phase and become more concentrated as the geothermal fluid ascends to the surface and boils, because the mass of liquid phase decreases as it boils. So the change of chloride concentration is actually a reflection of change of flowing steam fraction along the wellbore. It is possible to quantify this change and calculate back to the enthalpy of the preboiled fluid (Nicholson, 1993). Marini and Cioni (1985) proposed that enthalpy can be calculated from the change of chloride concentration based on the assumption that there was no loss of heat along the wellbore and the transformation of heat into kinetic energy is negligible, which can render the estimation of enthalpy inaccurate.

In our approach, enthalpy is calculated based on chloride mass conservation and total mass conservation without the no-heat-loss assumption. In fact, the approach provides a very useful way of estimating the heat loss along the wellbore. The method proposed here can provide better estimation of the enthalpy of two-phase flow, thus having more practical significance. In our method, chloride that is naturally in the geothermal fluid can be treated as a tracer to calculate enthalpy, without having to inject artificial chemical tracers. A comparison between the tracer injection method and our approach is summarized in Table 1-1.

Table 1-1: Comparison between tracer injection method and chloride tracer method.

	Requirement	**Advantage**	**Disadvantage**
Injecting chemical tracers	Precise metered tracer injection; Precise measurement of downstream tracer concentration;	Freedom in selecting tracer type; Relatively accurate measurement of mass flowrate and enthalpy	Chemical cost of injection; Precipitation of inorganic ion tracers in the pipe; Contamination of reservoir;
Using chloride naturally in the geothermal fluid as tracer	Precise measurement of chloride concentration at wellhead and in the downhole;	Save costs; No requirement for injection wells; Complete in shorter time;	Highly dependent on accuracy in chloride concentration measurement.

In this report, analytical models for enthalpy calculation based on chloride concentration are introduced. Enthalpy calculation with single feed zone and multiple feed zones are discussed separately. Different calculation procedures are illustrated under each scenario based on different assumptions.

Experimental studies were conducted to verify the analytical models and the associated assumptions. The experiments also provided estimation of the range of the error that was brought by the assumptions made in the models, so that the results calculated from the models could be calibrated, and the accuracy of the model could be enhanced.

Following the experiments, two-phase flow in the pipe with a feed zone was simulated using ANSYS Fluent to investigate the consistency between simulation results and experimental results. The simulated mixing process of the fluid from the feed zone with the fluid in the wellbore is visualized and compared to that from the experiment.

The analytical models are elaborated in Chapter 2 with examples and flow diagrams. Descriptions of the experiments and analysis of the experimental results are included in Chapter 3. Simulations conducted using ANSYS Fluent are described in Chapter 4.

Chapter 2

2. Analytical Models for Enthalpy Calculation Based on Chloride Concentration

In this chapter, calculation of enthalpy in two-phase geothermal wells is discussed. Typically, when the geothermal fluid ascends to the surface, it experiences a drop in pressure and temperature. As a result, phase changes, which are usually in the form of boiling, happen in the wellbore. Phase changes are associated with a change of chloride concentration along the wellbore, and mass balance of chloride can be applied to calculate the mass flow rate of steam and water, and the flowing enthalpy. The analytical models described in this chapter are based on this idea. However, the mass balance of chloride can be interrupted if there are more than one feed zone, so different models are proposed for single feed zone and multiple feed zones.

2.1. Enthalpy Calculation with Single Feed Zone

Chloride remains in the liquid phase and become more concentrated as the geothermal fluid boils along the wellbore, and the change of chloride concentration can be utilized to calculate the change of flowing steam fraction and enthalpy. Chloride mass balance and total mass balance of liquid and steam have to be considered for the quantification of this process.

In the first consideration, we only have one feed zone. It is assumed that the flow is steady and that the total mass of steam and liquid water is conserved. It is also necessary to assume that the chloride concentration in the gas phase is negligible so that the mass of chloride in the liquid phase is conserved as well.

First consider chloride mass balance:

$$d(Cl \cdot q_l) = 0 \tag{2-1}$$

where

- Cl is chloride concentration on a volumetric base, kg/m^3
- q_l is volumetric flow rate of the liquid phase, m^3/s

So if we measure the chloride concentration and the volumetric liquid flow rate at the surface, which are relatively easy to realize in practice, and the chloride concentration in the downhole, we can use Equation (2-1) to calculate the volumetric flow rate of liquid phase in the downhole, as illustrated by Equation (2-2) and (2-3).

$$\dot{m}_{cl} = Cl_{surface} \cdot q_{lsurface} = Cl_{surface} \cdot \frac{\dot{m}(1-x)}{\rho_l} \quad (2\text{-}2)$$

$$\dot{m}_{cl} = Cl_{downhole} \cdot q_{ldownhol} \quad (2\text{-}3)$$

where

- $\dot{m}_{cl}$ is mass flow rate of chloride, kg/s
- $Cl_{surface}$ is chloride concentration at the surface, kg/m^3
- $Cl_{downhole}$ is chloride concentration in the downhole, kg/m^3
- $q_{lsurface}$ is volumetric flow rate of the liquid phase at the surface, m^3/s
- $q_{ldownhole}$ is volumetric flow rate of the liquid phase in the downhole, m^3/s
- $\dot{m}$ is total mass flow rate, kg/s
- x is flowing steam fraction
- ρ_l is the density of liquid phase

Note that ρ_l is determined from surface pressure or surface temperature.

Total mass balance of steam and liquid water needs to be considered as well. The total mass balance is expressed in Equation (2-4).

$$d(\dot{m}) = d(\rho_l \cdot \frac{q_l}{1-x}) = 0 \quad (2\text{-}4)$$

where

- $\dot{m}$ is total mass flow rate, kg/s
- ρ_l is the density of liquid phase, kg/m^3
- q_l is volumetric flow rate of the liquid phase, m^3/s
- x is flowing steam fraction

ρ_l is determined from the temperature or pressure at the depth where q_l is measured or calculated. Now the downhole volumetric flow rate of the liquid phase calculated from Equation (2-2) and Equation (2-3) can be inserted into Equation (2-4) to calculate downhole flowing steam fraction, given that the total mass flow is measured at the surface.

$$x_{flowing} = 1 - \frac{q_{ldownhole}\,\rho_l}{\dot{m}} \quad (2\text{-}5)$$

Because thermodynamic properties of saturated water including steam enthalpy and liquid water enthalpy can be determined from temperature or pressure directly from the steam table, flowing enthalpy can be calculated from flowing steam fraction, as illustrated by Equation (2-6).

$$h_t = (1-x)h_l + xh_s \quad (2\text{-}6)$$

where

- h_t is total flowing enthalpy, kJ/kg
- h_l is the enthalpy of liquid water, kJ/kg
- h_s is the enthalpy of steam, kJ/kg

The input parameters required for this model include pressure at the surface, total mass flow rate at the surface, flowing steam fraction at the surface, chloride concentration at the surface, pressure in the downhole and chloride concentration in the downhole. All the input parameters are measurable. The output from the model is the flowing steam fraction and flowing enthalpy in the downhole. The structure is displayed in Table 2-1.

Table 2-1: Comparison between tracer injection method and chloride tracer method

	Surface	**Downhole**
Input	Pressure; Total mass flowrate m; Steam fraction x; Chloride concentration $Cl_{surface}$;	chloride concentration $Cl_{downhole}$; Pressure;
Output		**Flowing steam fraction x;** **Enthalpy h_t;**

Figure 2-1 is a schematic of the calculation procedure, including surface input, downhole input and the main equation part.

In an illustrative example, values for input parameters are given. Surface pressure was set to be 12.55 bar-a, and downhole pressure was 55.06 bar-a. The flowing steam fraction at the surface was 0.419. The total mass flow rate of steam and water at the surface was 70 kg/s. Chloride concentration at the surface was 0.4 kg/m^3, and chloride concentration in the downhole is 0.3 kg/m^3. The wellbore diameter is 0.3153m. Results are calculated through the process shown in Figure 2-1. The input values and results are shown in Table 2-2 and Figure 2-2.

Table 2-2: An example for enthalpy calculation with single feed zone

	Surface	**Downhole**
Input	Pressure: 12.55 bar-a; Total mass flowrate: 50kg/s; Steam fraction: 0.419; chloride concentration: 400g/m^3	chloride concentration: 300g/m^3; Pressure: 55.06 bar-a;
Output		Flowing steam fraction: 0.3214; **Enthalpy: 1701kJ/kg;**

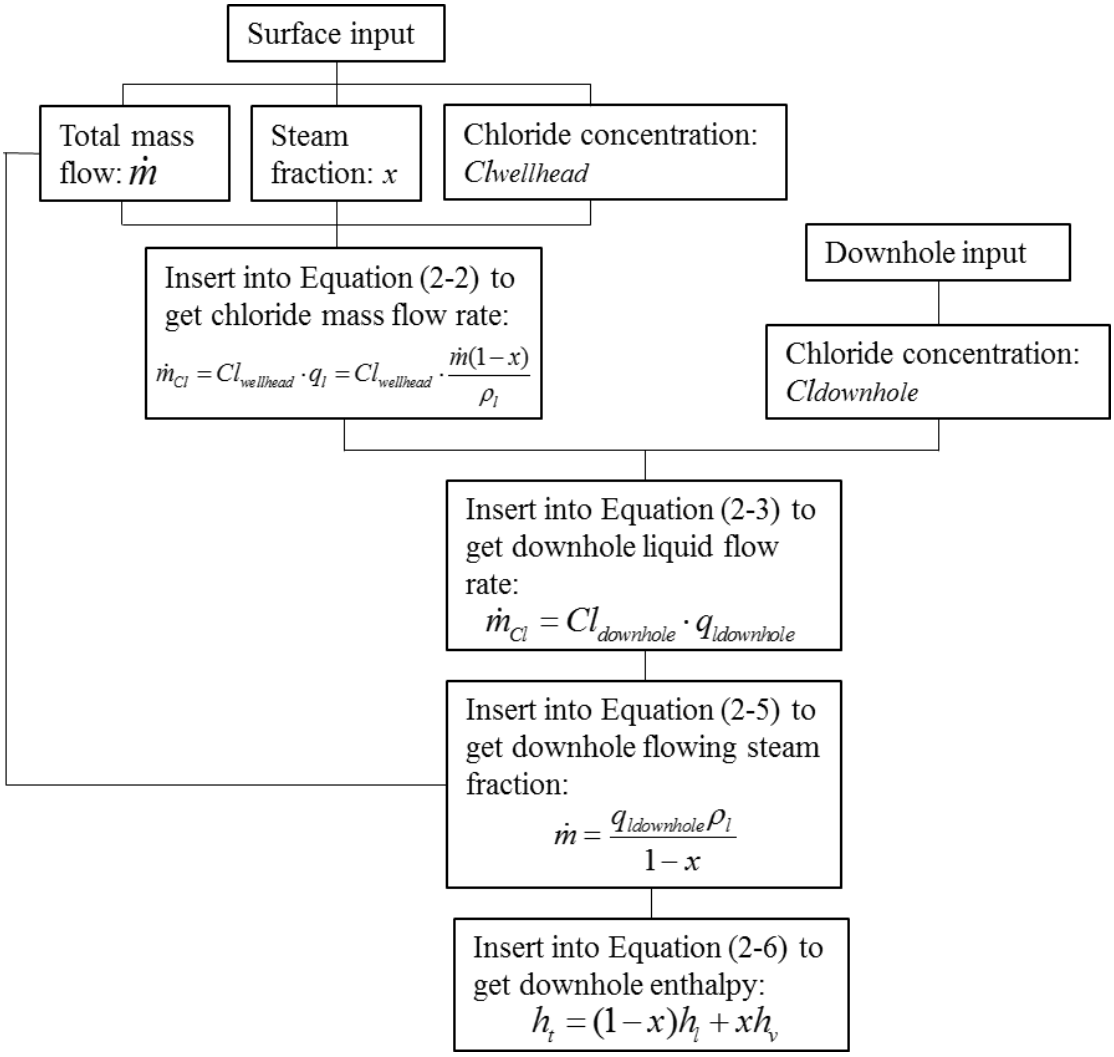

Figure 2-1: Flow diagram of enthalpy calculation process with single feed zone

Based on all the input parameters and the downhole enthalpy calculated following the procedure illustrated in Figure 2-1, we can estimate the heat loss along the wellbore. In the example, it was calculated that the heat loss is 64.75 kJ/kg, as shown in Figure 2-2.

In order to investigate the relationship between downhole chloride concentration and downhole enthalpy, we kept the input parameters in the example except downhole chloride concentration unchanged, and plotted the downhole flowing steam fraction along with downhole chloride concentration (Figure 2-3). As we can see from Figure 2-3, the flowing steam fraction increases with downhole chloride concentration, and this is because higher downhole chloride concentration implies that less liquid has boiled along the wellbore and the difference between downhole steam fraction and surface steam fraction is relatively small. The curve in Figure 2-3 indicates that the downhole steam fraction is not linearly related with downhole chloride concentration, and the nonlinear relationship can be inferred from Equation (2-3) and Equation (2-5).

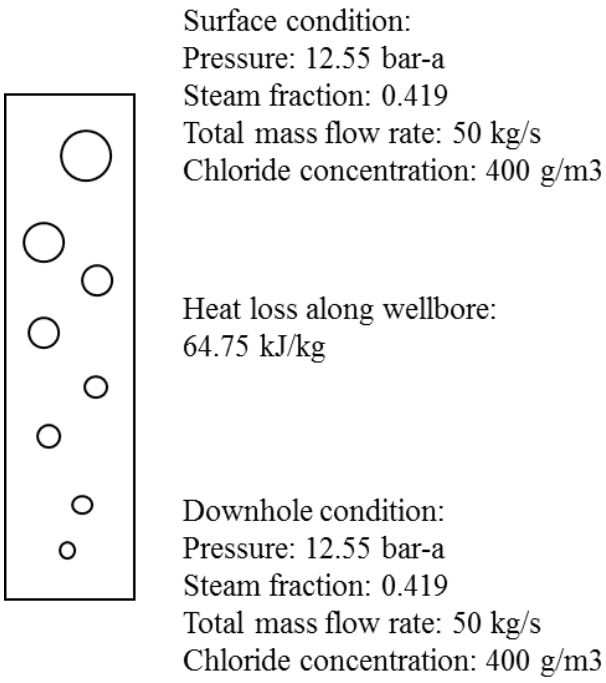

Figure 2-2: Schematic of the example for enthalpy and heat loss calculation with single feed zone

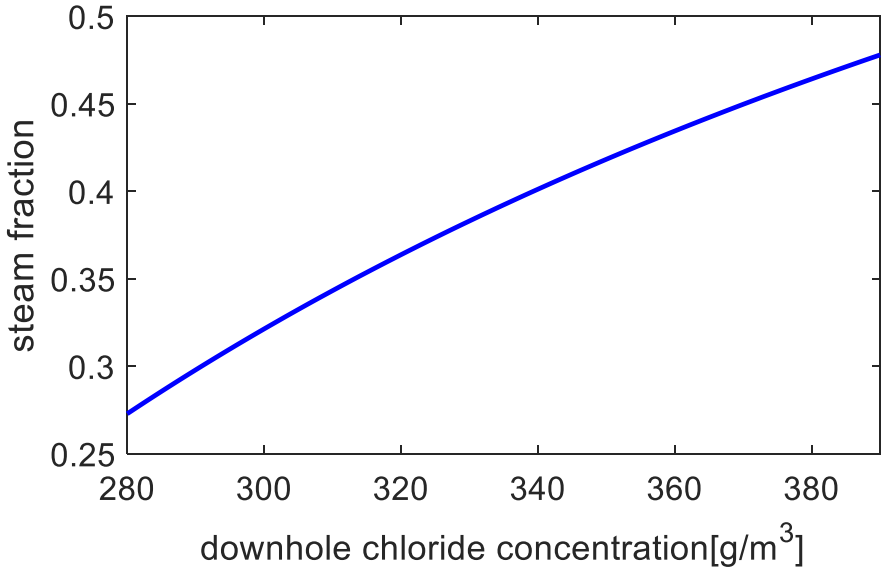

Figure 2-3 Relationship between downhole flowing steam fraction and downhole chloride concentration

The relationship between wellbore heat loss and downhole chloride concentration is shown in Figure 2-4 with all other input parameters kept constant. It can be seen from Figure 2-4 that wellbore heat loss increases with downhole chloride concentration, and the trend in Figure 2-4 is consistent with that in Figure 2-3. Higher downhole chloride concentration means larger downhole steam fraction and less vaporization in the

wellbore, but wellbore pressure drop is unchanged, so there must be more wellbore heat loss to make less vaporization happen. However, if the downhole chloride concentration is small enough, meaning that more liquid has boiled before reaching the surface, the calculated wellbore heat loss can become zero or even negative, and those values of downhole chloride concentration and associated values of downhole steam fraction are considered unphysical unless the fluid encounters increasing temperature as it ascends to the surface.

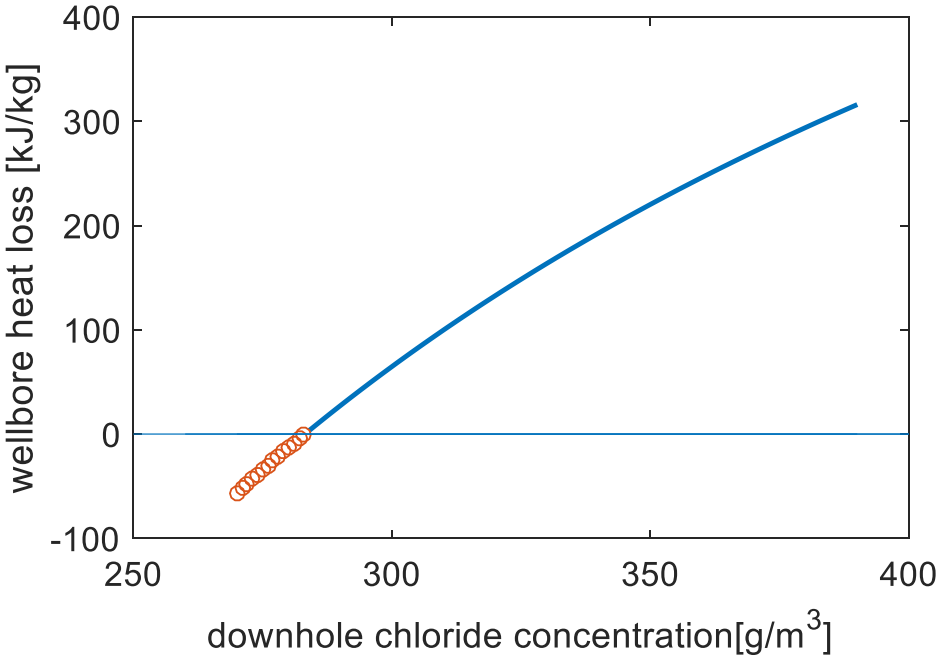

Figure 2-4 Relationship between wellbore heat loss and downhole chloride concentration

2.2. Enthalpy Calculation with Multiple Feed Zones

If there exist more than one feed zone along the wellbore, the calculation of enthalpy above all feed zones is same with the procedure described in Section 2.1. Nevertheless, if we want to estimate the amount of energy from each individual feed zone and the heat loss between the feed zones, more assumptions have to be made to adapt to the complication, because both chloride mass balance and total mass balance of geothermal fluids are disturbed. Inflowing geothermal fluid introduces not only steam and water but also chloride.

In this section, multiple feed zones are considered in three different cases and different models are introduced. In the first case, the feed zone introduces only liquid, and the fluid below the feed zone can be either single-phase flow or two-phase flow. In the second case, the feed zone introduces both steam and liquid, but the fluid below the feed zone contains only liquid phase. In the third case, the feed zone introduces both steam and liquid, and the fluid below the feed zone also contains both steam and liquid.

The equipment used for chloride concentration measurement need to be designed to be small and flexible, making it possible to align the measurement tool against the wall of the wellbore. As a result, it is reasonable to assume that the chloride concentration measured at the very entrance of the feed zone could represent the chloride concentration of the inflowing geothermal fluid, as shown in Figure 2-5. This assumption is discussed in more detail in Chapter 4. In Figure 2-5, the small black rectangles represent the tools for chloride concentration measurement. Device 1 measures the chloride concentration above the feed zone, and device 2 measures the chloride concentration below the feed zone. Device 3 measures the chloride concentration right at the entrance of the feed zone. Zero chloride concentration indicates the passing of gas phase. Similarly, chloride concentration of a finite amount indicates the passing of liquid phase. In Figure 2-5, m_2 is total mass flow rate below the feed zone. m_{in} is total mass flow rate from the feed zone, and m is total mass flow rate above the feed zone.

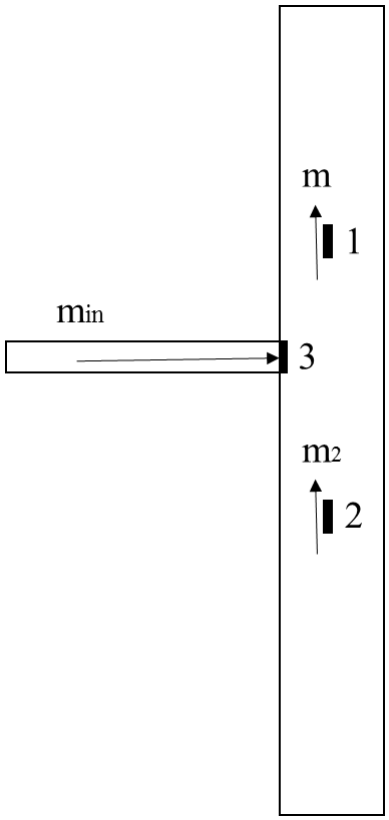

Figure 2-5 Schematic of chloride concentration measurement with multiple feed zones

If the concentration measured by Device 3 is always larger than zero, Case 1 should be considered. If the concentration measured by Device 3 is sometimes zero but the concentration measured by device 2 is always zero, Case 2 should be considered. If the concentration measured by Devices 2 and 3 both sometimes have zero values, Case 3 should be considered.

Case 1, 2 and 3 are discussed separately in Section 2.2.1-Section 2.2.3.

2.2.1. Enthalpy Calculation in Case 1

A schematic of Case 1 is shown in Figure 2-6. The feed zone introduces only liquid phase.

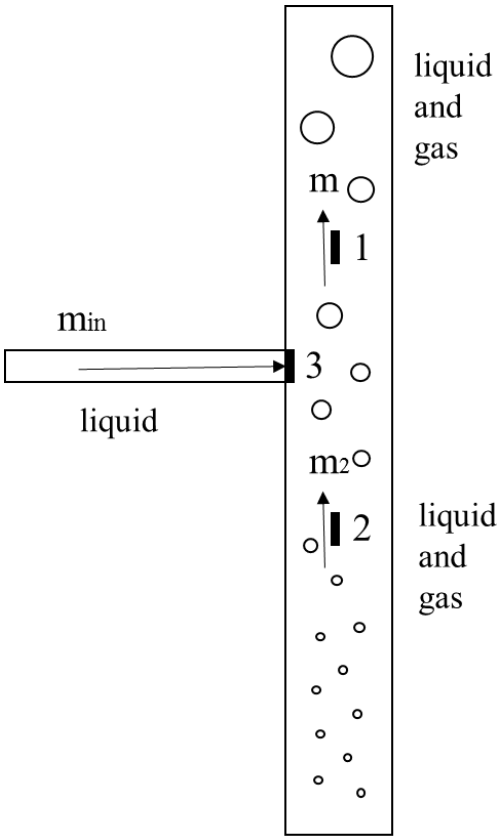

Figure 2-6 Schematic of Case 1 with multiple feed zones

The total chloride mass flow rate equals the chloride mass flow rate from the feed zone and the chloride mass flow rate below the feed zone. The updated chloride mass balance is shown in Equation (2-7).

$$q_{lin} \cdot Cl_{in} + (q_l - q_{lin}) \cdot Cl_{below} = q_l \cdot Cl_{above} \tag{2-7}$$

where,

- q_{lin} is volumetric flow rate of the liquid phase from the feed zone, m^3/s
- Cl_{in} is the chloride concentration of the liquid from the feed zone, kg/m^3
- q_l is total volumetric flow rate of the liquid phase, i.e. the liquid flow rate above the feed zone, m^3/s
- Cl_{below} is the chloride concentration of the liquid below the feed zone, kg/m^3
- Cl_{above} is the chloride concentration of the liquid above the feed zone, kg/m^3

Cl_{in}, Cl_{below} and Cl_{above} can be measured, as shown in Figure 2-6. q_l can be calculated through the process discussed previously in Section 2.1, so the only unknown variable is q_{lin}, which can be calculated from Equation (2-6). After determining the flow rate from the feed zone, we can calculate the flow rate below the feed zone (Equation (2-7)), so that we do not need to measure it.

$$q_{lbelow} = q_l - q_{lin} \tag{2-8}$$

where,

- q_{lbelow} is volumetric flow rate of the liquid phase below the feed zone, m^3/s

Another parameter we need to know is the flowing steam fraction below the feed zone. In Case 1, the boiling process happens in the wellbore, and the introduced geothermal fluid from the feed zone contains no steam, which allows us to calculate the total mass flow rate below the feed zone from the total mass flow rate above the feed zone (Equation (2-9)).

$$\dot{m}_{below} = \dot{m} - q_{lin} \cdot \rho_{lin} \tag{2-9}$$

where,

- $\dot{m}_{below}$ is total mass flow rate of steam and water below the feed zone, kg/s
- $\dot{m}$ is total mass flow rate, kg/s
- ρ_{lin} is the density of the liquid from the feed zone, kg/m^3

Note that ρ_{lin} can be determined from the pressure measured at the depth of the feed zone.

Then we can calculate the flowing steam fraction using the total mass flow rate obtained from Equation (2-9) and the liquid flow rate obtained from Equation (2-8):

$$x = \frac{\dot{m}_{below} - q_{lbelow}\rho_{lbelow}}{\dot{m}_{below}} \tag{2-10}$$

where,

- ρ_{lbelow} is the density of the liquid below the feed zone, kg/m^3

Similarly, ρ_{lbelow} is determined from the pressure measured at the same depth with the tool 2 in Figure 2-6.

After calculating flowing steam fraction using Equation (2-10), we can repeat the same process as in the previous calculation in Section 2.1. The enthalpy below the feed zone can be calculated easily using Equation (2-6), and the enthalpy from the feed zone is simply the difference between the total enthalpy above the feed zone and that below the feed zone.

The calculation process for Case 1 is shown in Figure 2-7.

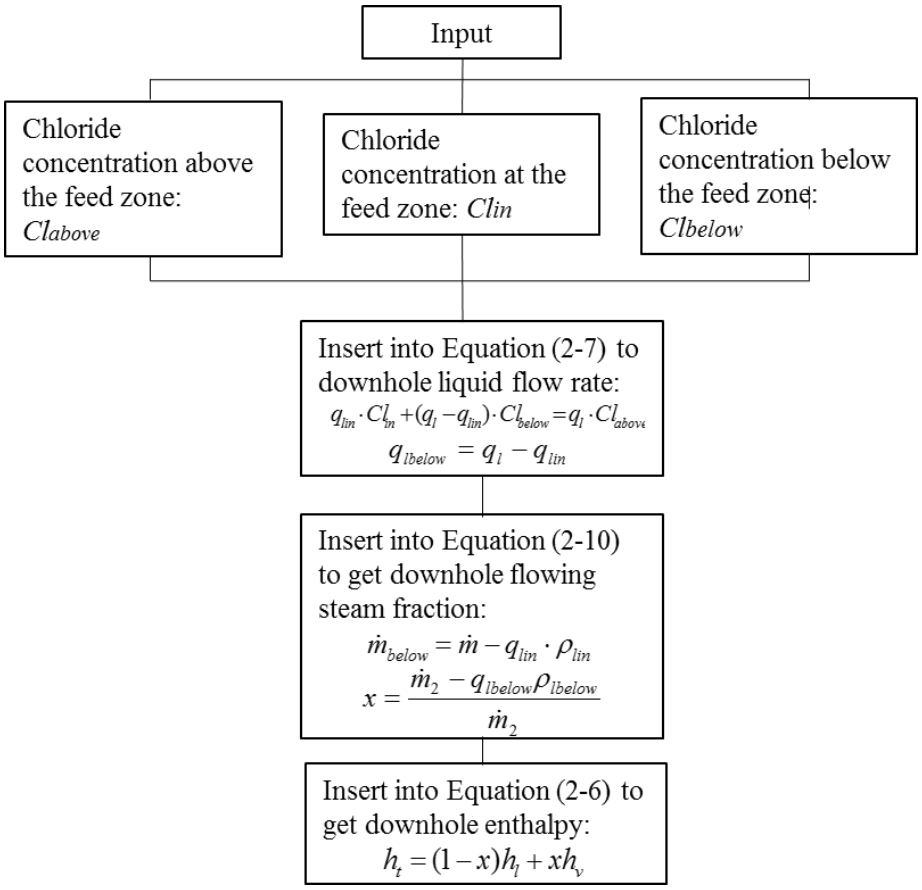

Figure 2-7 Flow diagram of enthalpy calculation process in Case 1

An example of enthalpy calculation for Case 1 is provided. In the example, the downhole condition and surface condition are the same as those in the example in Section 2.1. The chloride concentration of the liquid from the feed zone is 280 g/m^3, the chloride concentration of the liquid below the feed zone is 320 g/cm^3. The parameters in this example are displayed in Table 2-3. In this example, the liquid flow rate from the feed zone is calculated to be 0.0221 m^3/s, which corresponds to a mass flow rate of 16.9 kg/s. The liquid flow rate below the feed zone is calculated to be 17.1 kg/s. The flowing steam fraction below the feed zone is 0.8085, and the total enthalpy of the fluid below the feed zone is 2482.5 kJ/kg. Enthalpy of the liquid from the feed zone is 1185.3 kJ/kg.

In Figure 2-8, the chloride concentration above and below the feed zone are kept constant, while the chloride concentration measured at the feed zone is changed continuously. The rest of the parameters in the example remain constant. We can observe from Figure 2-8 that the liquid flow rate from the feed zone increases with chloride concentration measured at the feed zone, because in the example, higher chloride concentration at the feed zone indicates larger contribution of mass from the feed zone. The total enthalpy of the fluid below the feed zone also increases with the chloride

concentration at the feed zone, because larger liquid flow rate from the feed zone means smaller liquid flow rate below the feed zone, thus larger steam fraction and total enthalpy.

Table 2-3: An example for enthalpy calculation in Case 1

	Surface	Downhole (above feed zone)	At the depth of feed zone	Downhole (below feed zone)
Input	Pressure: 12.55 bar-a; Total mass flowrate: 50kg/s; Steam fraction: 0.419; Chloride concentration: 400g/m^3	Chloride concentration: 300g/m^3; Pressure: 55.06 bar-a;	Chloride concentration: 280 g/m^3;	Chloride concentration: 320 g/m^3;
Output		Flowing steam fraction: 0.3214; Enthalpy: 1701 kJ/kg;	Liquid flow rate: 16.9 kg/s; Enthalpy: 1185.3 kJ/kg	Flowing steam fraction: 0.8085; Enthalpy: 2482.5 kJ/kg

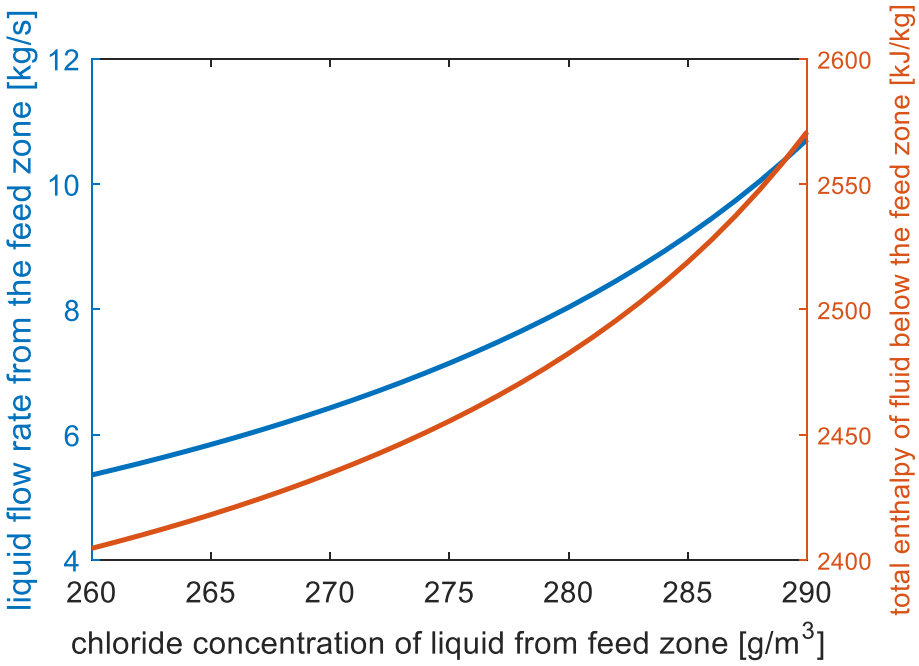

Figure 2-8 Relationship between liquid flow rate from the feed zone and the chloride concentration measured at the feed zone in Case 1

2.2.2. Enthalpy Calculation in Case 2

A schematic of Case 2 is shown in Figure 2-9.

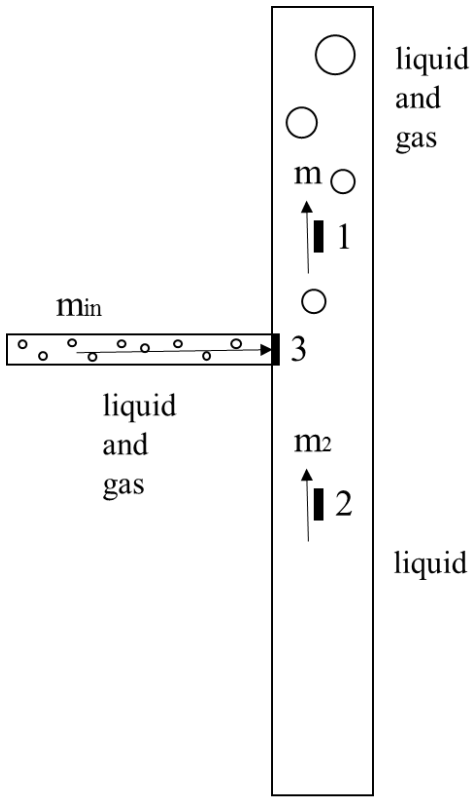

Figure 2-9 Schematic of Case 2

In Case 2, the feed zone introduces both liquid and gas, but the flow below the feed zone contains only liquid, so the enthalpy below the feed zone can be determined by measuring pressure or temperature. The enthalpy above the feed zone can be calculated by following the process discussed in Section 2.1. The enthalpy introduced by the feed zone is simply the difference between the enthalpy above the feed zone and the enthalpy below the feed zone.

The example for Case 2 is similar to that for Case 1, as shown in Table 2-4. The enthalpy of the liquid below the feed zone is 1185 kJ/kg, while the enthalpy introduced by the feed zone is 1967.8 kJ/kg, which is much higher than that in Case 1, because the fluid from the feed zone contains more steam this time. In this example, the flowing steam fraction from the feed zone is 0.4877, and this number is calculated using the procedure described in Section 2.2.1. We can calculate the liquid flow rate from and below the feed zone, and thus the steam flow rate from the feed zone, given that the fluid below the feed zone contains only liquid.

Table 2-4: An example for enthalpy calculation in Case 2

	Surface	**Downhole (above feed zone)**	**At the depth of feed zone**	**Downhole (below feed zone)**
Input	Pressure: 12.55 bar-a;	Chloride concentration:	Chloride	Chloride

	Total mass flowrate: 50kg/s; Steam fraction: 0.419; Chloride concentration: 400g/m^3	300g/m^3; Pressure: 55.06 bar-a;	concentration: 280 g/m^3;	concentration: 320 g/m^3;
Output		Flowing steam fraction: 0.3214; Enthalpy: 1701 kJ/kg;	Steam fraction: 0.4877; Enthalpy: 1967.8 kJ/kg	Enthalpy: 1185 kJ/kg

2.2.3. Enthalpy Calculation in Case 3

Figure 2-10 shows a schematic of Case 3

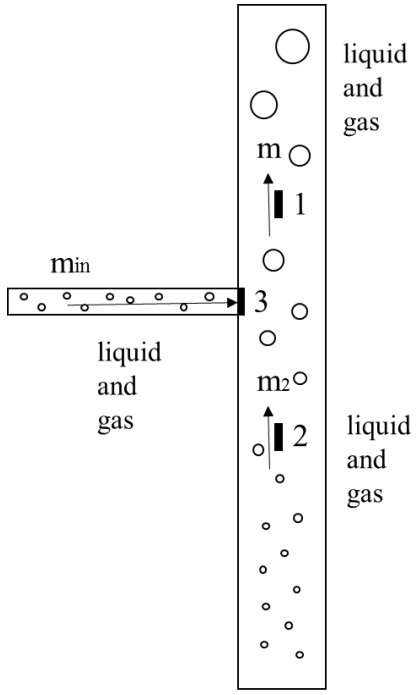

Figure 2-10 Schematic of Case 3

Case 3 is the most difficult, because both the feed zone and the flow below the feed zone have liquid and gas. As the chloride remains in the liquid phase, the gas introduced by the feed zone does not affect chloride mass balance, so the same process as in Section 2.2.1 can be still followed to determine the liquid flow rate from and below the feed zone. However, liquid flow rate is not sufficient to determine the enthalpy below the feed zone, because gas flow rate is also needed to calculate the flowing steam fraction. Because the amount of gas introduced by the feed zone is unknown, it is hard to know the gas flow rate below the feed zone. Two approaches of determining enthalpy in Case 3 are discussed here. The first approach involves direct measurement of gas flow rate and void

fraction. The second approach applies energy balance and only requires measurement of temperature at the inlet of the feed zone. Calculation procedures based on both approaches are explained, but the second approach is considered more practical.

2.2.3.1 The first approach of determining enthalpy in Case 3

According to previous study, both fiber optic (Atalay, 2008) and electrodes for resistivity measurement (Juliusson, 2006) satisfy the resolution requirement, and void fraction and gas velocity are measurable using the tools introduced in the literature. The procedure to calculate enthalpy based on combination of chloride concentration measurement, void fraction measurement and gas velocity measurement is illustrated in Figure 2-11.

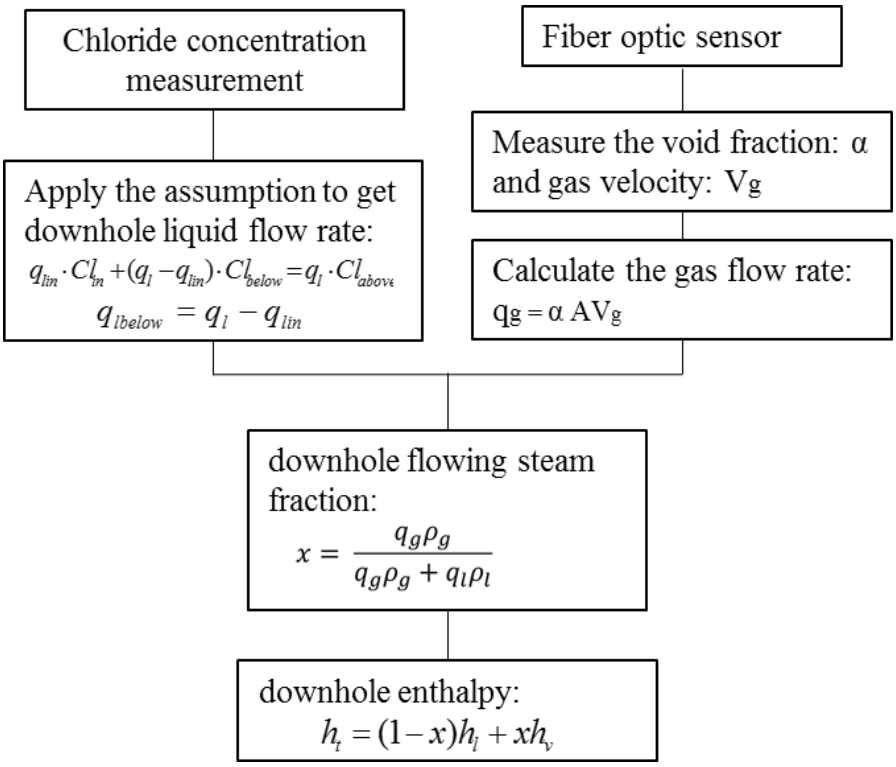

Figure 2-11 calculate enthalpy based on combination of chloride concentration measurement, void fraction measurement and gas velocity measurement

However, measuring gas velocity and void fraction accurately in the downhole is still a difficult job. Application of fiber optic and high-resolution electrodes in real geothermal wells has not been tested yet.

2.2.3.2 The second approach of determining enthalpy in Case 3

As an alternative approach, we can consider measure the temperature of the inflowing geothermal fluid from the feed zone, which requires a flexible temperature measurement tool, and then apply the energy balance to calculate flow rates from the feed zone.

According to the literature (Grant, 1982; Hyndman, 1979), such temperature measurement tools have been used in practice.

The mass balance of liquid phase is discussed in Case 1 and Case 2, where we can use the chloride concentration measured at the entrance of the feed zone to calculate the liquid flow rate from and feed zone and the liquid flow rate below the feed zone. The problem remaining is determining the steam flow rate from and below the feed zone, which can be achieved through the energy balance by measuring the temperature at the entrance of the feed zone.

The saturated steam enthalpy and liquid enthalpy can be determined by measuring the temperature. Denote the steam enthalpy from the feed zone as h_{sin}, the liquid enthalpy from the feed zone as h_{lin}, the steam enthalpy below the feed zone as h_{s0}, the liquid enthalpy below the feed zone as h_{l0}, the steam enthalpy above the feed zone as h_{s1}, and the liquid enthalpy above the feed zone as h_{l1}. The energy balance is written in Equation (2-11).

$$m_{lbelow}h_{l0} + m_{sbelow}h_{s0} + m_{lin}h_{lin} + m_{\sin}h_{\sin} = m_{labove}h_{l1} + m_{sabove}h_{s1} \tag{2-11}$$

where

- m_{lbelow} is the liquid mass flow rate below the feed zone, kg/s
- m_{sbelow} is the steam mass flow rate below the feed zone, kg/s
- m_{lin} is the liquid mass flow rate from the feed zone, kg/s
- $m_{\sin}$ is the steam mass flow rate from the feed zone, kg/s
- m_{labove} is the liquid mass flow rate above the feed zone, kg/s
- m_{sabove} is the steam mass flow rate above the feed zone, kg/s

From Case 1 and Case 2, we know that m_{lbelow} and m_{lin} can be calculated using Equation (2-9) and Equation (2-10). m_{labove} and m_{sabove} are known from the single-feed-zone calculation, as illustrated in Section 2.1. So the unknowns in Equation (2-11) are $m_{\sin}$ and m_{sbelow}. The mass balance of the steam phase is shown in Equation (2-12).

$$m_{sbelow} + m_{\sin} = m_{sabove} \tag{2-12}$$

Combining Equation (2-11) and Equation (2-12), we can solve for $m_{\sin}$ and m_{sbelow}, and then use m_{sbelow} and m_{lbelow} to calculate the flowing enthalpy below the feed zone by Equation (2-6). The calculation process is illustrated in Figure 2-12.

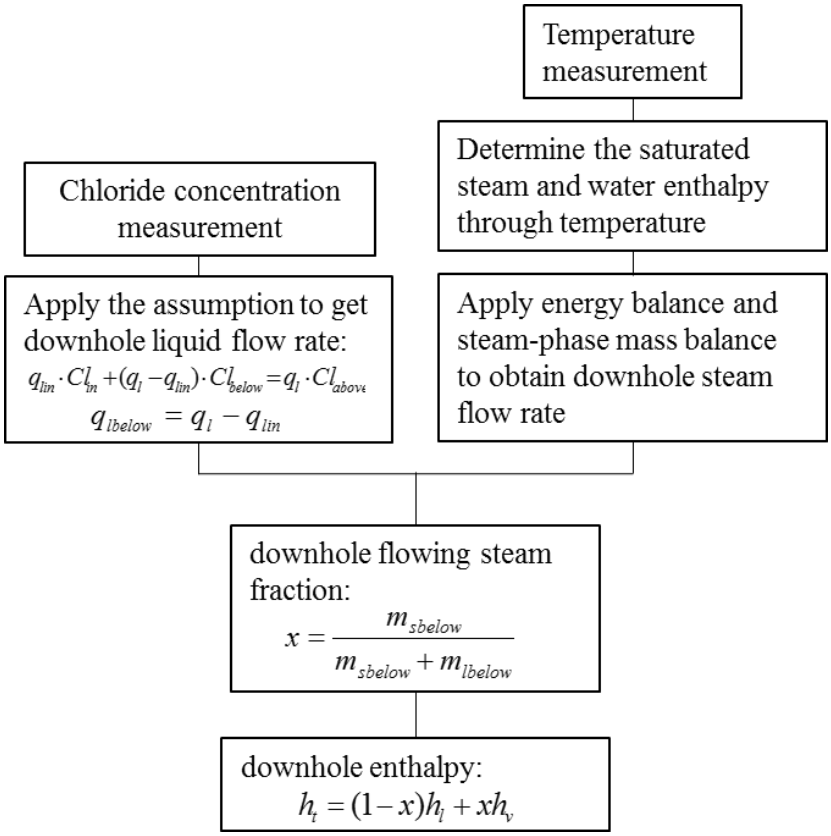

Figure 2-12 calculate enthalpy based on combination of chloride concentration measurement and temperature measurement

An example of applying energy balance and mass balance to calculate enthalpy in Case 3 is provided, as shown in Table 2-5. The example follows the calculation process shown in Figure 2-12.

In the example, total mass flow rate above the feed zone is 50 kg/s with a total flowing enthalpy of 1701 kJ/kg. The liquid flow rate above the feed zone is 34 kg/s, and the steam flow rate above the feed zone is 16 kg/s. The steam fraction above the feed zone is 0.3214. The liquid mass flow rate from the feed zone is 16.9 kg/s, and the liquid mass flow rate below the feed zone is 17.1 kg/s. The mass liquid flow rates are same as those in Case 1 and Case 2. The temperature measured at the feed zone is 260 °C, indicating a steam enthalpy of 2796.6 kJ/kg and a liquid enthalpy of 1134.8 kJ/kg. The temperature measured below the feed zone is 280 °C, indicating a steam enthalpy of 2779.8 kJ/kg and a liquid enthalpy of 1236.7 kJ/kg.

By following the calculating process shown in Figure 2-12, we could calculate that the steam flow rates from and below the feed zone are calculated to be 3.15 kg/s and 12.92 kg/s respectively. The total flowing enthalpy from the feed zone is 1396 kJ/kg. The total flowing enthalpy below the feed zone is 1901 kJ/kg.

Table 2-5: An example for enthalpy calculation in Case 3

	Surface	Downhole (above feed zone)	At the depth of feed zone	Downhole (below feed zone)
Input	Pressure: 12.55 bar-a; Total mass flowrate: 50kg/s; Steam fraction: 0.419; Chloride concentration: 400g/m^3	Chloride concentration: 300g/m^3; Pressure: 55.06 bar-a;	Chloride concentration: 280 g/m^3; Temperature: 260 °C	Chloride concentration: 320 g/m^3; Temperature: 280 °C
Output		Flowing steam fraction: 0.3214; Enthalpy: 1701 kJ/kg;	Steam fraction: 0.1571; Enthalpy: 1396 kJ/kg	Steam fraction: 0.4304 Enthalpy: 1901 kJ/kg

2.3. Chapter Summary

This chapter elaborates analytical models for enthalpy calculation in two-phase geothermal wells based on chloride concentration. Enthalpy calculation with single feed zone and multiple feed zones are discussed, and examples are provided under different scenarios. The following conclusions can be drawn:

1. The downhole enthalpy of the two-phase flow in geothermal wells can be determined by measuring surface chloride concentration and downhole chloride concentration.

2. In the case of single feed zone, the physical model for calculating downhole enthalpy based on chloride concentration involves chloride mass balance and total mass balance of gas and liquid.

3. In the case of multiple feed zones, an assumption has to be made that the chloride concentration in the liquid entering from the feed zone is measurable. The model to calculated liquid flow rate from the feed zone is described.

4. Gas flow rate below the feed zone also needs to be determined if both the flow from feed zone and the flow below the feed zone contain two phases. Two approaches can be applied to determine gas flow rate below the feed zone. In the first approach, void fraction and gas flow rate are measured to determine the flow rate of the gas phase and the enthalpy. In the second approach, temperature at the entrance of the feed zone is measured and energy balance is applied to calculate the steam flow rate and the flowing enthalpy below the feed zone. The second approach is more feasible in practice.

5. Future development on the chloride concentration measuring tool to achieve higher frequency of measurement is a necessary task for wells with multiple feed zones. Such a chloride tool has the potential to measure void fraction and gas velocity, thus providing important information for enthalpy calculation.

Chapter 3

3. Experimental Study of Measuring Enthalpy with a Downhole Tool

The analytical model elaborated in Chapter 2 is based on chloride concentration measurement in the downhole. The tool used for chloride concentration measurement, which was developed by Sandia National Laboratories, is introduced in this chapter.

Experimental study with the tool was conducted to support the analytical model. The tool was calibrated before the experiments, and the calibration result was consistent with the calibration result from Sandia National Laboratories. The ability of the tool to measure chloride concentration in two-phase wells was demonstrated through experiments.

The assumption that the chloride concentration measured at the inlet of the feed zone can represent the exact concentration of the liquid from the feed zone plays an important role in the model with multiple feed zones and influences the accuracy of the model. In the experiments, the validity of this important assumption was examined by measuring chloride concentration with the tool around the inlet. In order to visualize the mixing procedure, experiments with dye tracers from the feed zone were also conducted. Videos of the dye tracer experiment were analyzed with computer vision methods to understand the extent of color penetration and the influence of the in-flowing fluid from the feed zone.

3.1. Introduction of the Downhole Tool

Cieslewski et al. (2016) and Corbin et al. (2017) introduced a wireline tool containing a ruggedized electrochemical sensor for real-time tracer concentration measurement. The tool was developed by Sandia National Laboratories. Details of fabrication and materials of the tool were illustrated by Cieslewski et al. (2016) and Corbin et al. (2017).

In order to satisfy the specific purpose of measuring chloride concentration, the tool was assembled with the chloride-ion selective sensing element. The lab-scale tool is 29.3 cm in length and 2.65 cm in diameter. The tool consists of three electrodes: a chloride-ion selective electrode (Cl-ISE), a solid state bimodal pellet reference electrode and a graphite ground reference electrode.

The electrical potential difference between the Cl-ISE and the reference electrode is an indicator of chloride concentration. A photo of the tool immersed in saturated sodium chloride solution is shown in Figure 3-1. The electrodes at the bottom of the tool and the connection wires are shown in Figure 3-2.

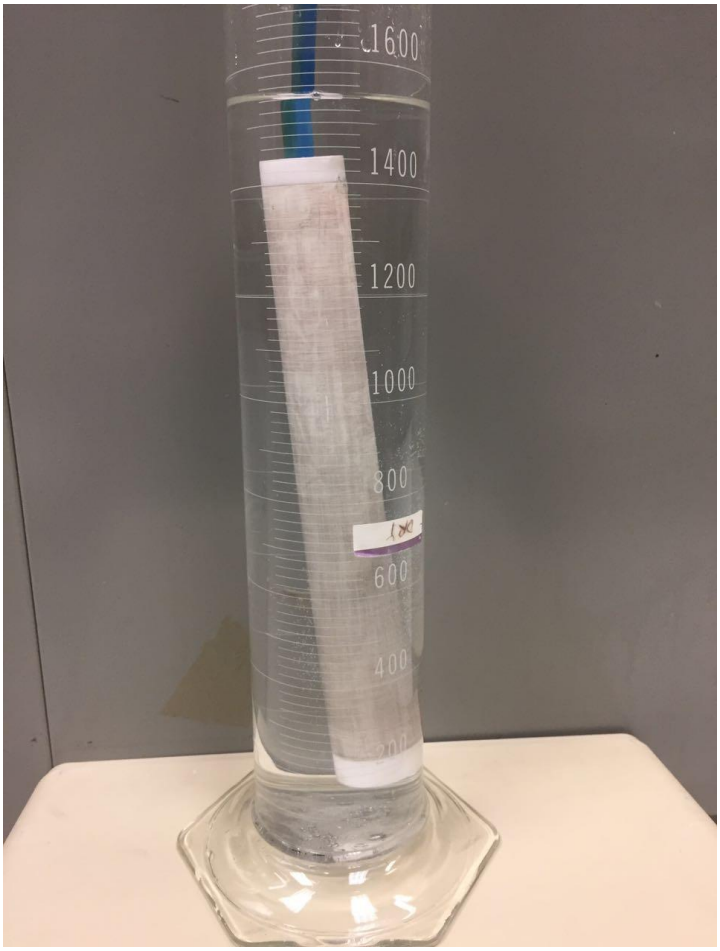

Figure 3-1 Photo of the downhole tool developed for chloride concentration measurement

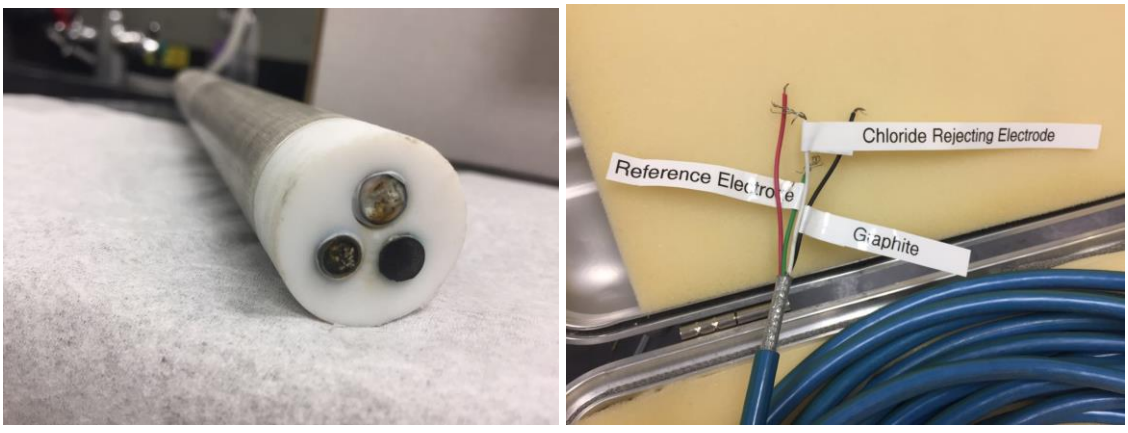

Figure 3-2 Electrodes (left) and connection wires (right) of the tool.

Note the chloride rejecting electrode Figure 3-2 is the same as the Cl-ISE. The three electrodes in Figure 3-2 are spaced evenly apart.

3.2. Calibration of the Downhole Tool

In the experiment, the potential difference between the Cl-ISE and the reference electrode was measured in sodium chloride solution with different concentrations for calibration purpose. Calibration experiments were conducted at both Sandia National Laboratories and Stanford Geothermal Laboratory.

The calibration from Sandia included four test groups and provided distributions of measurements and prediction bounds at different chloride concentration levels. The distribution provided by Sandia has an overall standard deviation of 0.03584 Volts.

Another group of calibrations was done at Stanford. The tool was immersed in saturated sodium chloride solution in the laboratory for 24 hours before the experiment to allow for rehydration of the tool. In order to formulate sodium chloride solution with very low concentrations (5×10^{-6} mol/L -0.01 mol/L), a water tank containing 100.8 L of water was used in the experiment. Sodium chloride solution with higher concentrations (0.05 mol/L-0.95 mol/L) were formulated in the graduated cylinder shown in Figure 3-1. An electrical balance (Sartorius SECORA5102-1S) with a resolution of 0.01 g was used to measure the weight of sodium chloride mass. Sodium chloride was added incrementally into the solution to create gradually increasing concentrations. In the experiment, the potential difference between the Cl-ISE and the reference electrode was measured with a digital multimeter (Commercial Electric MS8301A). The Cl-ISE was connected to the Common (COM) jack through the black test lead, and the reference electrode was connected to the mAVΩ jack through the red test lead. The potential difference between the two electrodes was measured under the DC Voltage mode within the range of 200 mV. Measurements were taken after the sodium chloride was completely dissolved and the reading from voltmeter became stable. The time required to reach equilibrium is longer at lower concentrations than at higher concentrations.

The calibration results from Sandia and from Stanford are shown in Figure 3-3. In Figure 3-3, the blue dots represent data collected at Sandia, and the red dots represent data collected at Stanford. It can be seen from Figure 3-3 that both calibrations were completed with a well-defined linear relationship, and the calibration result obtained at Stanford was consistent with that obtained at Sandia.

The relationship between the chloride concentration and the voltage was found by fitting the calibration results:

$$-\log(M) = 46.87 \cdot Voltage - 2.9846 \tag{3-1}$$

where,

- M is chloride concentration, mol/L
- *Voltage* is the electrical potential difference between the Cl-ISE and the reference electrode, V

The regression has an R^2 of 0.99.

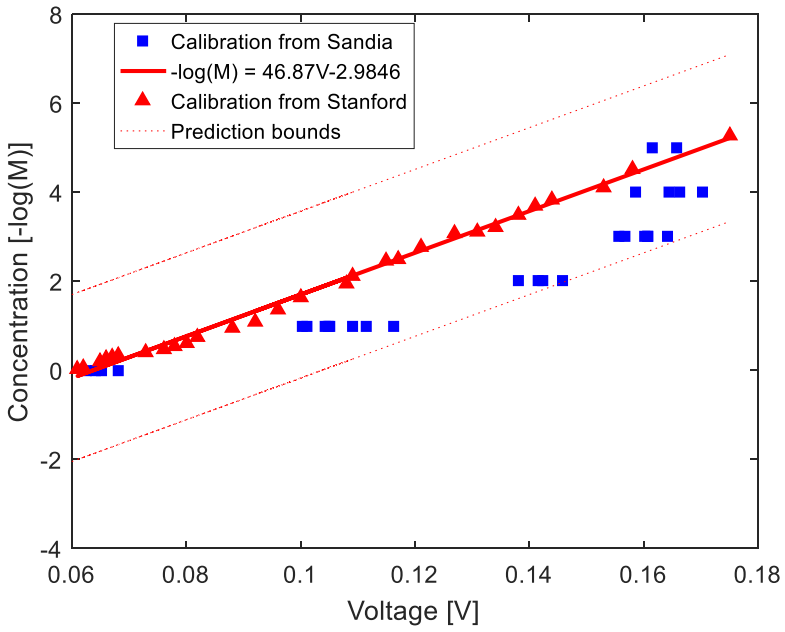

Figure 3-3 Calibration of the tool

The relationship between chloride concentration and voltage shown by Equation (3-1) was applied in later experiments for chloride concentration measurements.

3.3. Measurement of Chloride Concentration in Two-phase Bubble Flow

The accuracy of enthalpy estimation is highly dependent on the precise measurement of chloride concentration in the downhole, and it is necessary to study the performance of the tool in two-phase turbulent flow.

An artificial well that can flow two-phase fluid was used for chloride concentration measurement. A photo of the well is shown in Figure 3-4. Different elements of the artificial well are marked by the red rectangles in Figure 3-4. The well is 5.5 inch in diameter and 71.3 inch in height. A water tank with a storage of about 200 L was placed at the bottom of the well. Three circulation pipes were used to connect the top of the well and the water tank, so that water could be circulated through the system after being pumped into the well from the bottom. The water pump was powered by a capacitor-start motor (Dayton 6K232C) with a power of 1 hp. An in-house compressed air source supplied air to the system. The air also entered the well from the bottom. A flow mixer located at the bottom of well was used to fully mix the water and the air. The well is equipped with three injection ports to simulate feed zones. Sensors and tools could be placed into the well from the top. A schematic of the system is shown in Figure 3-5. The flow loop was originally designed and constructed by Kumar (1995).

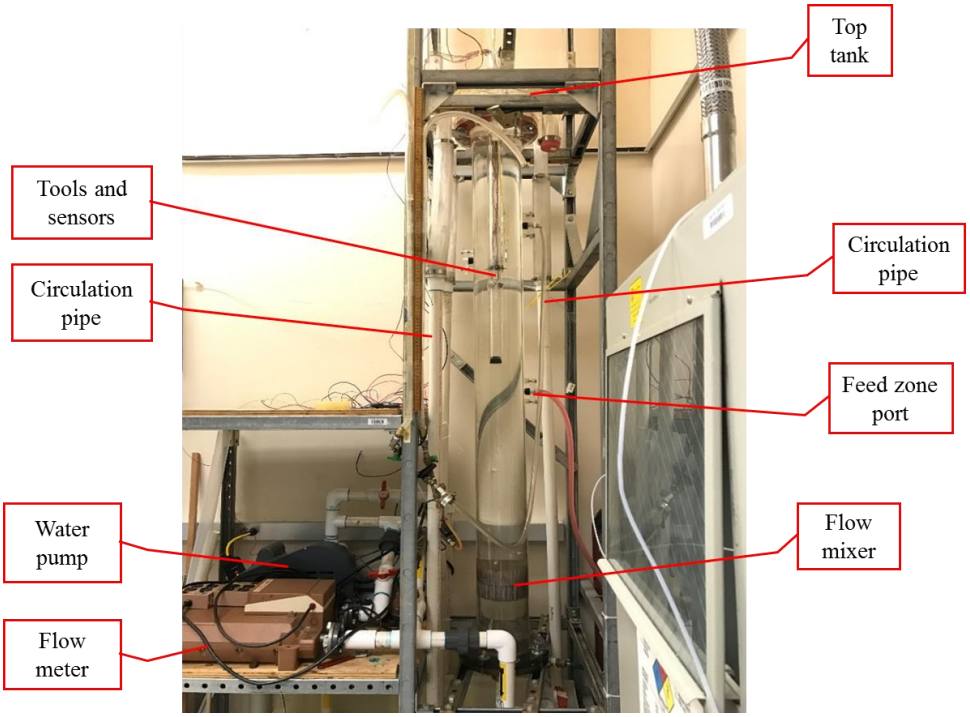

Figure 3-4 Photo of the artificial well

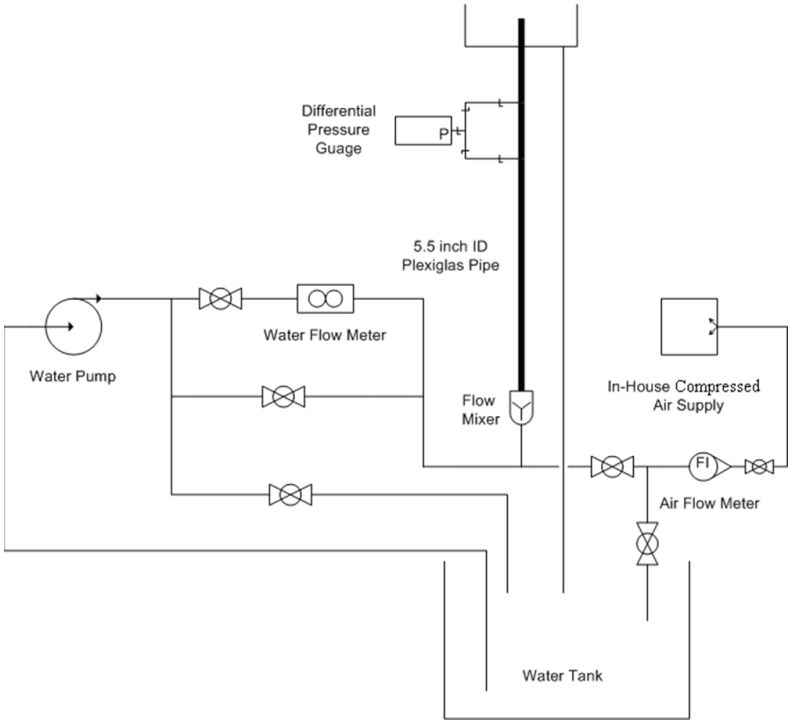

Figure 3-5 A schematic of the flow loop (Kumar 1995)

The tool was placed into the well using an iron rod that was 60 cm in length and 5 mm in diameter. By attaching the tool to the iron rod, it was feasible to control the location of the tool in the well. A photo of the tool in two-phase bubble flow is shown in Figure 3-6.

Figure 3-6 Photo of the tool in two-phase flow

Chloride concentration was measured in the flowing well in both single-phase (liquid) flow and two-phase flow. The liquid flow speed and flow rate was measured by recording the time when the liquid entered the wellbore and the time when the liquid level reached the top of the wellbore. The total length and diameter of the wellbore was known, so that the liquid speed and flow rate could be calculated. The gas flow rate was measured using a spinner flow meter (King Instrument 7205-6061-A). The liquid flow speed was about 0.3 m/s, and the liquid flow rate was about 6.7 kg/s. The experiments were conducted with constant liquid flow rate but varying gas flow rate, ranging from 1 standard cubic feet per minute (SCFM) to 6 SCFM.

The chloride concentration in the liquid phase was increased incrementally from 0.115 mol/L to 0.832 mol/L by adding sodium chloride into the water tank at the bottom of the well. At each chloride concentration, the measurements were taken with gradually increasing gas flow rates. The actual chloride concentration was obtained by measuring the weight of sodium chloride added into the water tank and the volume of water in the water tank. The total water volume was 150.3 L, and the cumulative sodium chloride mass was increased from 1.01 kg to 7.31 kg.

Data of chloride concentration measured under each gas flow rate is shown in Figure 3-7. The unit slope line in Figure 3-7 indicates the actual chloride concentration of the liquid phase, and deviation from the unit slope means measurement error occurs at the corresponding point.

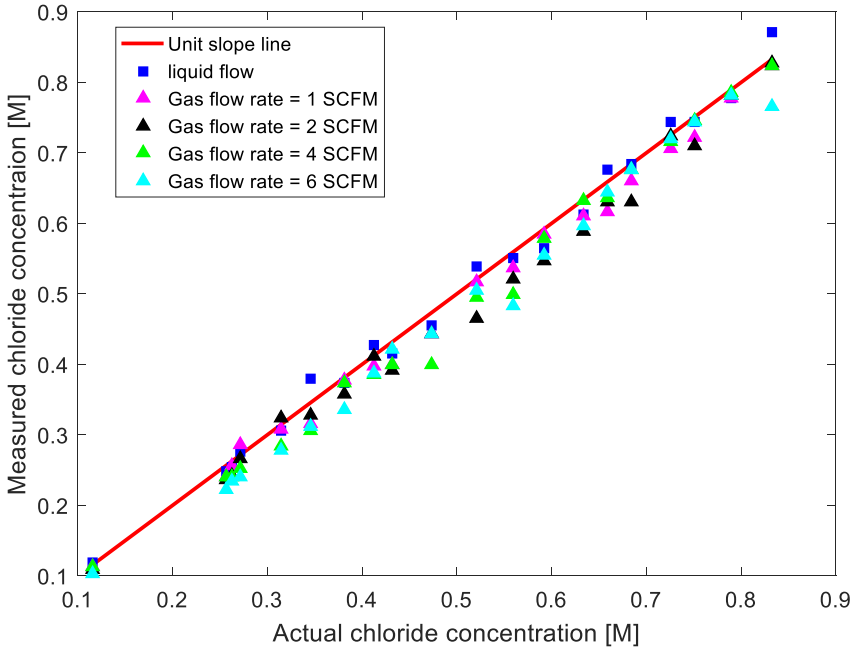

Figure 3-7 Measurements of chloride concentration in single-phase and two-phase flows

As we can see from Figure 3-7, the measurement data points are relatively consistent with the unit slope line, and measurement in single-phase (liquid) flow is more accurate than that in two-phase flow.

It was found that the chloride concentration measured in two-phase flow was slightly lower than that measured in single-phase flow, because the tiny bubbles in two-phase flow increased the voltage between the electrodes of the tool, and thus decreased the apparent chloride concentration obtained from the voltage. It can be seen from Figure 3-2 that the distance between the electrodes are small, so only gas bubbles with very small diameters could affect the voltage measurement. Note that in the experiment, the flow mixer at the bottom of the well, which was originally designed to make the flow in the wellbore more homogeneous, actually helped creating more bubbles with very small diameters.

Figure 3-8 shows the average relative errors in chloride concentration measurements with different gas flow rates. Although a trend can be observed that the average relative error increases with the gas flow rate, the average relative error with high gas flow rate (6 SCFM) is still acceptable (less than 7%).

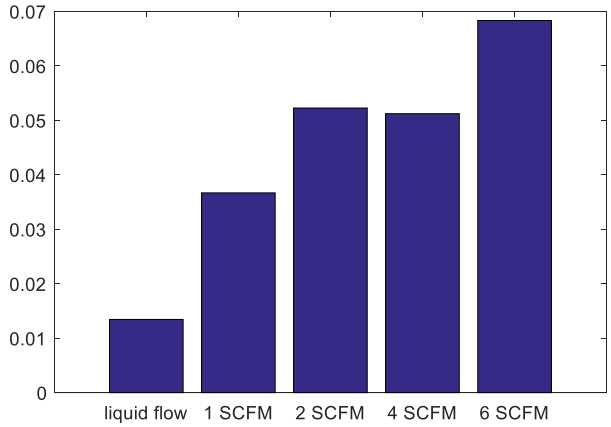

Figure 3-8 Average relative error with different gas flow rates

Using the example shown in Table 2-2, we can calculate that if the downhole chloride concentration is underestimated by 7%, the final downhole enthalpy calculated using the analytical model would be underestimated by 4.82%. The calculation results using underestimated chloride concentration are shown in Table 3-1. Note that the downhole chloride concentration in Table 2-2 is 300 g/m^3, while in Table 3-1 it is 279 g/m^3.

Table 3-1: An example for enthalpy calculation using underestimated chloride concentration

	Surface	**Downhole**
Input	Pressure: 12.55 bar-a; Total mass flowrate: 50kg/s; Steam fraction: 0.419; chloride concentration: 400g/m^3	chloride concentration: 279g/m^3; Pressure: 55.06 bar-a;
Output		Flowing steam fraction: 0.2704; **Enthalpy: 1619 kJ/kg;**

The relationship between the relative error in chloride concentration measurement in the downhole and the relative error in enthalpy estimation from the analytical model is shown in Figure 3-9. The range of relative error in chloride concentration measurement, which is 0.01-0.07, was obtained from the experiments. The relationship between the two types of relative error was found by fitting the data points in Figure 3-9.

$$\varepsilon_{enthalpy} = 0.695 \cdot \varepsilon_{chloride} - 0.0008 \tag{3-1}$$

where

- $\varepsilon_{enthalpy}$ is relative error in enthalpy estimation based on the analytical model;
- $\varepsilon_{chloride}$ is relative error in chloride concentration measurement in the downhole;

The regression has a R^2 of 0.997.

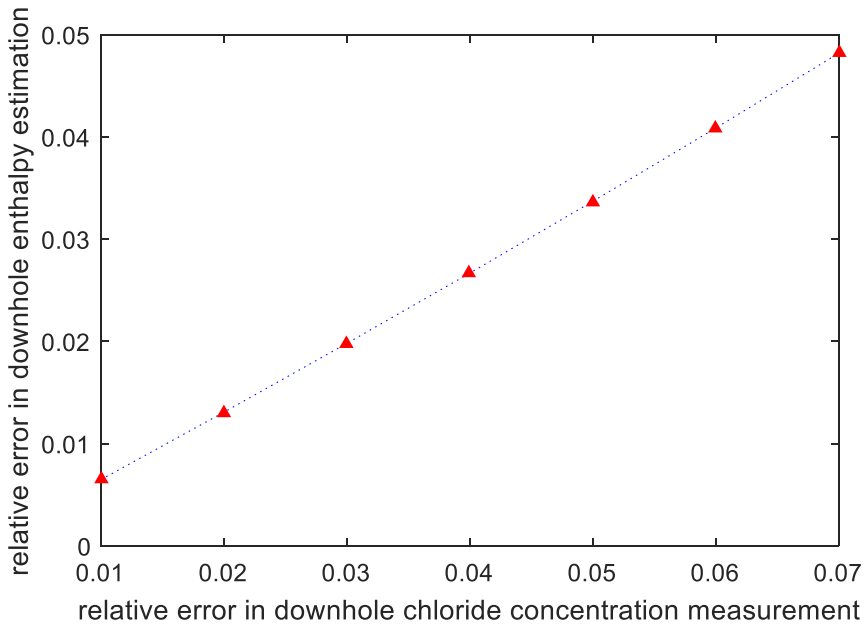

Figure 3-9 Relationship between the relative error in chloride concentration measurement in the downhole and the relative error in enthalpy estimation

Figure 3-9 and Equation (3-1) allow for direct evaluation of error in enthalpy estimation based on error in chloride concentration measurement. Note that the relationship given by Equation (3-2) is only valid when error in chloride concentration measurement is within the range of 0.01-0.07. In addition, Figure 3-8 shows that error in chloride concentration measurement is related with gas flow rate. Therefore, it is possible to adjust chloride concentration and enthalpy estimation using the gas flow rate calculated from the analytical model. The effect of gas phase on the measurement error is expected to be smaller when the gas is in the form of slug or annular flow where lower quantities of small-diameter gas bubbles are entrained within the flow.

3.4. Measurement of Chloride Concentration of Liquid from the Feed Zone

As elaborated in Chapter 2, our analytical model relies on a key assumption that the chloride concentration measured at the inlet of the feed zone can represent the actual chloride concentration of the liquid from the feed zone. This assumption is important for determining downhole enthalpy with multiple feed zones, because measuring the chloride concentration from the feed zone allows us to calculate the liquid flow rate from the feed zone based on chloride mass balance. It is necessary to study the mixing behavior of the fluid from the feed zone with the fluid in the well.

The experiment discussed in this section was conducted using the artificial well shown in Figure 3-4. The feed zone port marked in Figure 3-4 was connected to another water pump (Little Giant Pump NK-2) so that liquid could be injected into the feed zone port from another water tank. The power of the water pump used to inject liquid is 1/40 hp. The storage of the small water tank used to store feed zone liquid is 8.26 L. The experiment was divided into two groups. In the first group, 110.98 g sodium chloride was

added into the feed zone liquid, so that the chloride concentration of the feed zone liquid was 0.23 mol/L. The liquid in the large tank (i.e. the liquid flowing in the well before the injection) was tap water. The tool was attached to an iron rod and placed into the well from the top. The location of tool in the tool could be controlled using the iron rod, so that chloride concentration could be measured at different distances from the inlet (from 0 to 5 cm). Figure 3-10 shows a schematic of layout of the experiment.

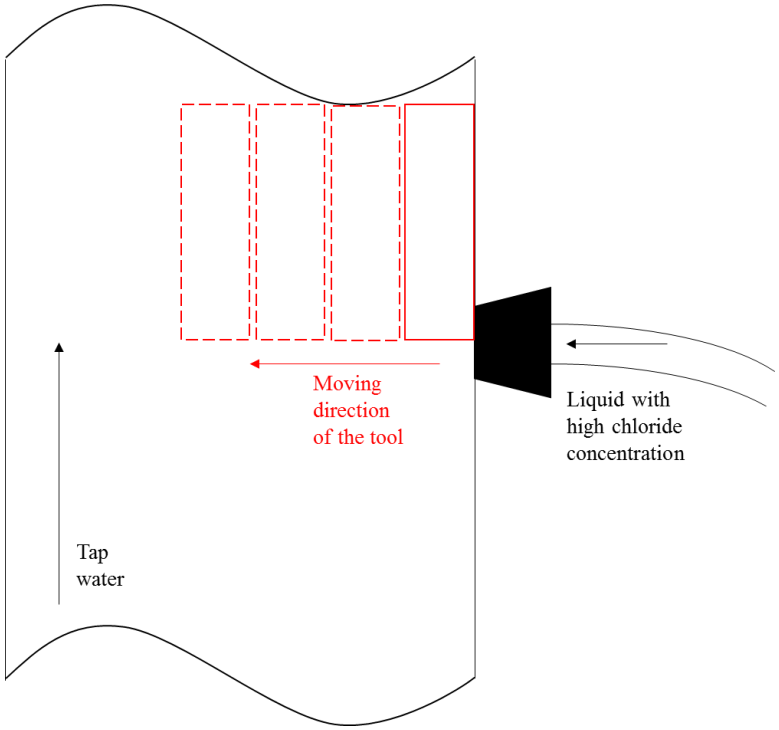

Figure 3-10 Measure chloride concentration at different distances from the inlet

The flow in the mixing zone is turbulent, so the measurement taken at each distance from the inlet was unstable and displayed a distribution. The distribution of chloride concentration in the mixing zone was studied by taking multiple measurements at each location. In the experiment, about 50 measurements were taken at each distance from the inlet.

In the second group of experiments, a total of 294.46 g sodium chloride was added into the feed zone liquid, and the chloride concentration of the feed zone liquid was 0.61 mol/L. Similarly, about 50 measurements were taken at each distance from the inlet. The experiment procedure was same with that in the first group of experiment.

The distribution of chloride concentration in the mixing zone is shown in Figure 3-11 and Figure 3-12. Figure 3-11 is the box plot of the distribution and Figure 3-12 is the violin plot of the distribution. The box plot shows the mean value, P10 and P90 of the chloride concentrations measured at different distances. The violin plot shows the estimated mathematical distributions of chloride concentration at different distances based on given measurements. The red lines in Figure 3-11 and Figure 3-12 indicate the chloride

concentrations of the liquid from the feed zone. Figure 3-11 (a) and Figure 3-12 (a) show the distributions obtained from the first group of experiments, and Figure 3-11 (b) and Figure 3-12 (b) show the distributions obtained from the second group of experiments.

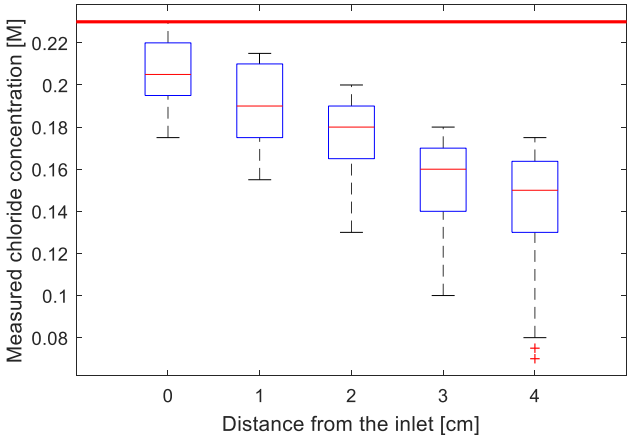

(a) Feed zone concentration 0.23 mol/L

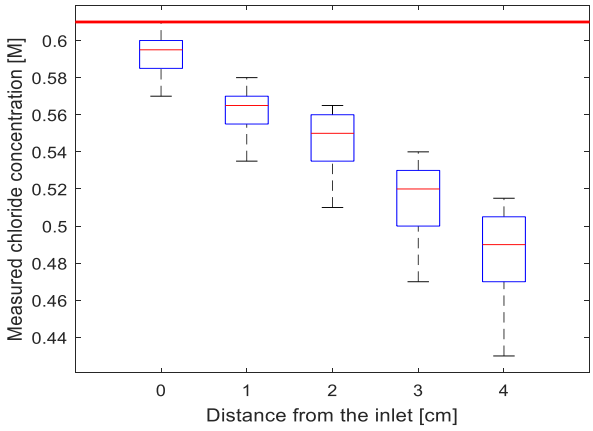

(b) Feed zone concentration 0.61 mol/L

Figure 3-11 Box plot of concentration distribution in the mixing zone

Several observations can be made from Figure 3-11 and Figure 3-12:

- From the box plot, it can be seen that the average chloride concentration decreases with the distance from the inlet, which is expected because of the dilution of chloride ions in the mixing zone.
- The length of the box, which indicates the range of the data, increases with the distance from the inlet. In the violin plot, the length of the violin increases with the distance from the inlet. This means measurements taken at longer distance from the inlet have larger variation, because the mixing zone is wider at locations further from the inlet. This phenomenon was also observed in the dye tracer experiment introduced in Section 3.5.
- Higher chloride concentration in the mixing zone can be considered as an influence from the feed zone, and lower concentration can be considered as an

influence from the flow below the feed zone. It can be seen from the violin plot that the violins are wider in the upper part and narrower in the lower part, which means the measurement location is more frequently influenced by the fluid from the feed zone than the fluid below the feed zone. This was also observed in the dye tracer experiment.

- If the tool is placed closely against the wall of the well, as shown in Figure 3-6, it is feasible to obtain the concentration value from the feed zone relatively accurately. In Figure 3-11 and Figure 3-12, the top of the distribution at distance 0 touches the red line, meaning the highest concentration measured is very close to the true concentration of the liquid from the feed zone. Even though in some cases it is hard to align the tool against the wall of the well, we can adjust our measurement based on the distance from the inlet using Figure 3-11 and 3-12.

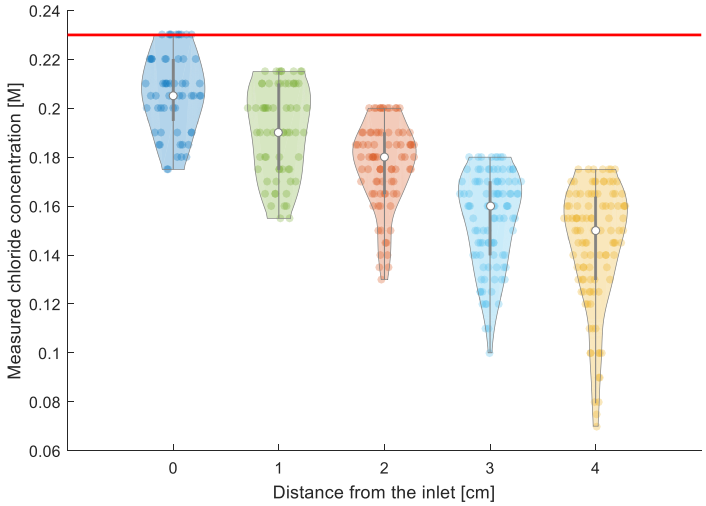

(a) Feed zone concentration 0.23 mol/L

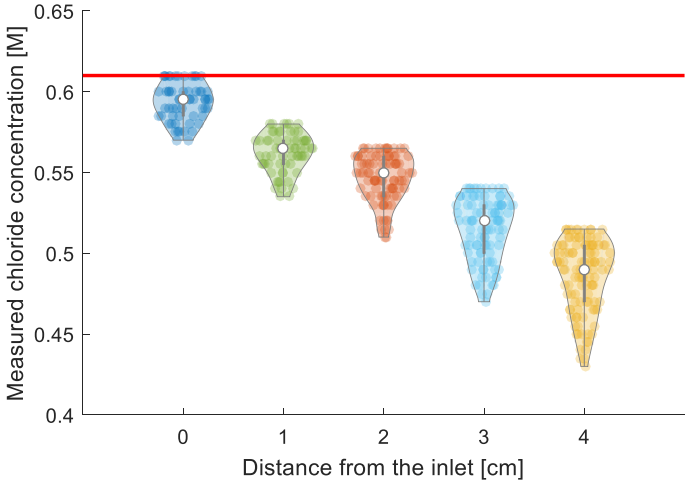

(b) Feed zone concentration 0.61 mol/L

Figure 3-12 Violin plot of concentration distribution in the mixing zone

3.5. Dye Tracer Experiment

In Section 3.4, the chloride concentration distribution in the mixing zone is illustrated quantitatively, and the experiment results show that the highest chloride concentration measured at the inlet of the feed zone can represent the chloride concentration of the liquid from the feed zone, which supports the assumption made in the analytical model.

In order to further study the influence of the fluid from the feed zone and estimate the extent of penetration of the fluid from the feed zone into the wellbore, the mixing zone was visualized through a set of dye tracer experiments, which are introduced in this section. It is useful to measure the penetration distance because it allows for estimation of the zone where chloride concentration of the liquid from the feed zone can be measured relatively accurately. Studying the mixing procedure also has practical significance in perspective of fluid mechanics.

In the dye tracer experiments, the liquid injected into wellbore from the feed zone port was dyed with red color tablets (Bright Dye 101100 Fluorescent Industrial Red). Each tablet was able to dye 60 gallons of water. The liquid flowing in the well was not dyed, so that the mixing zone could be visualized by the red color.

The dyed liquid was injected with varying flow rate, ranging from 20 ml/s to 200 ml/s. The injection rate in the dye tracer experiments means the flow rate from the feed zone. The shape of the mixing zone and the penetration distance were observed under each injection rate. Videos were taken to record the mixing procedure with low injection rate and high injection rate.

When the injection rate was low, the mixing zone oscillated with the turbulent flow in the well, and the penetration distance varied within a range. The range of penetration depended on the injection rate. Figure 3-13 provides examples of different shapes of the mixing zone when the injection rate was low.

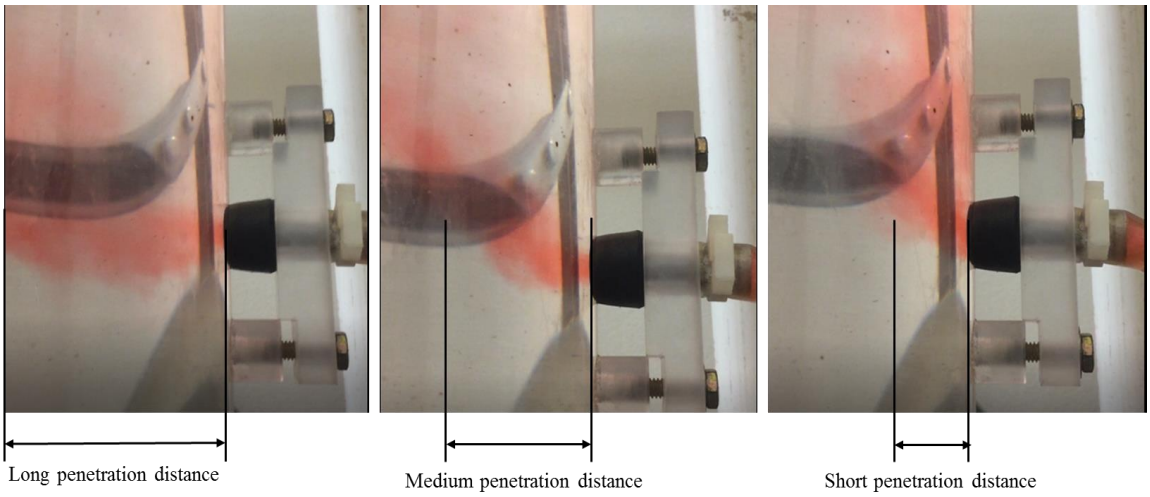

Figure 3-13 Different shapes of the mixing zone with low injection rate

In Figure 3-13 and Figure 3-14, the red area is the mixing zone.

When the injection rate was high, the shape of the mixing zone was more stable. When the injection rate was higher than about 80 ml/s, the maximum penetration distance was equal to the well diameter. Figure 3-14 shows an example of the penetration process with high injection rate.

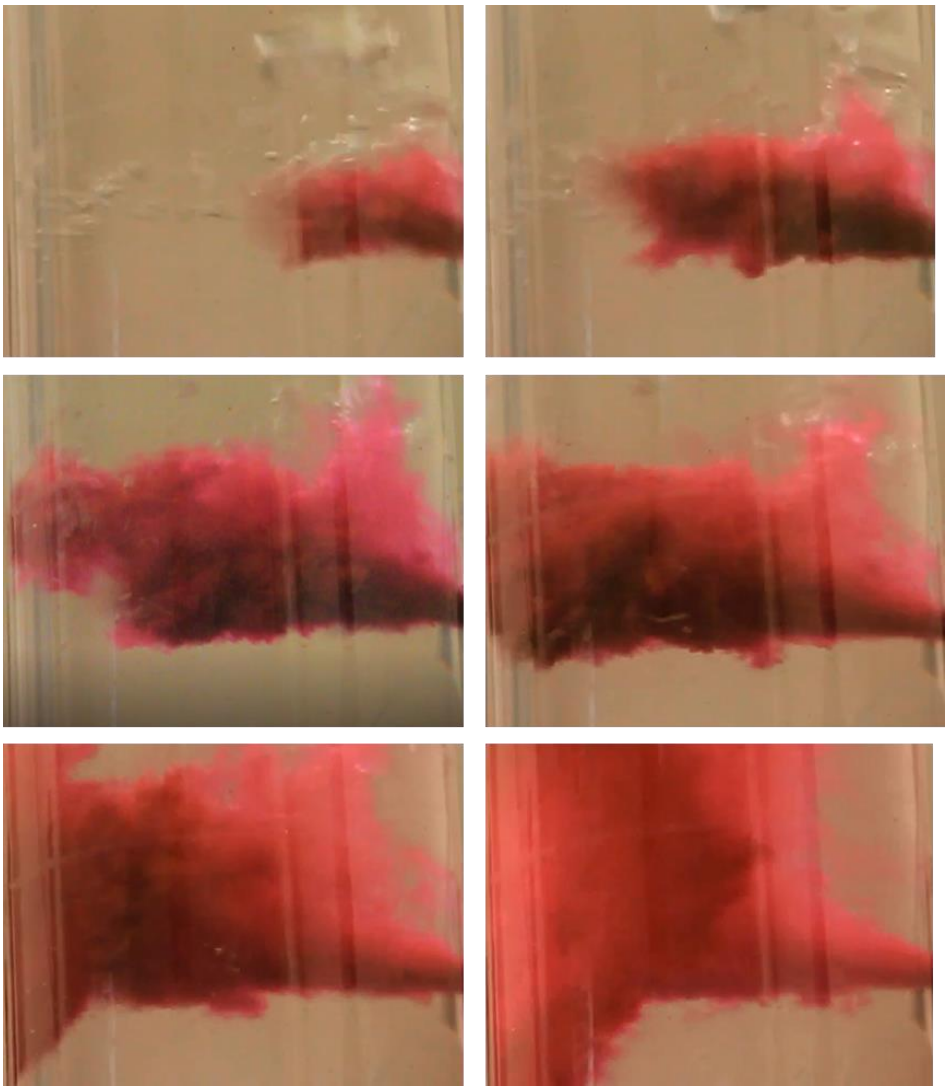

Figure 3-14 Penetration process with high injection rate. The time interval between the images is about 0.1 s.

It is necessary to study the distribution of the penetration distance under different injection rates. If the penetration distance is short, the measurement tool needs to be placed very close to the inlet to obtain an accurate measurement, which is feasible but not very easy. However, if the short penetration distance happens at a low frequency, it is safe to relax the requirement on measurement distance and simplify the measurement.

3.5.1. Computer Vision Treatment of Experiment Results

In order to study the oscillation pattern of the mixing zone statistically under low injection rate and the relationship between the penetration distance and the injection rate, videos from the experiments were segmented into frames and analyzed quantitatively.

Each frame of the video was transformed into a binary figure to simplify the analysis process, which was achieved by setting a red color threshold based on the pixel histogram. According to the RGB (Red, Green and Blue) model, a wide range of colors can be created by combing the three additive primary colors, which are red, green and blue. Each frame of the video was treated as a RGB image and stored in the form of a m×n×3 matrix. The third dimension of the matrix defines the primary color components for each pixel. The first array in the third dimension defines the red component in the pixel. The histogram of red components in the pixels is shown in Figure 3-15, and the threshold was set based on the histogram. In this case, the lower threshold was set to be 150, and the upper threshold was set to be 200.

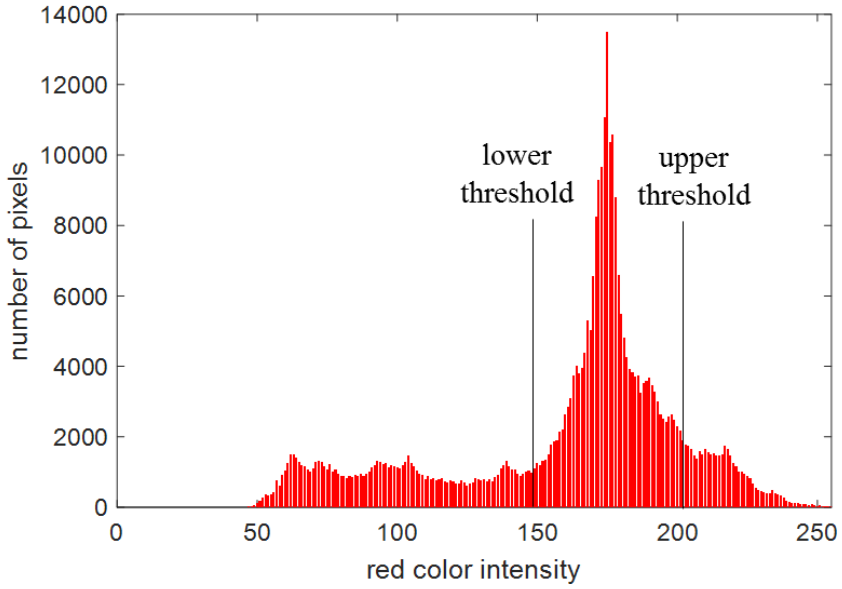

Figure 3-15 Histogram of red components in a RGB image

The pixels that fall between the lower threshold and the upper threshold and the pixels that fall out of the range were separated, so that the image was transformed into a black-white binary image.

The red area (the mixing zone) in the original image was marked by the black area in the binary image. It is much easier to study the distribution of the mixing zone and the penetration distance using the binary images. Comparison between original images and the binary images is shown in Figure 3-16.

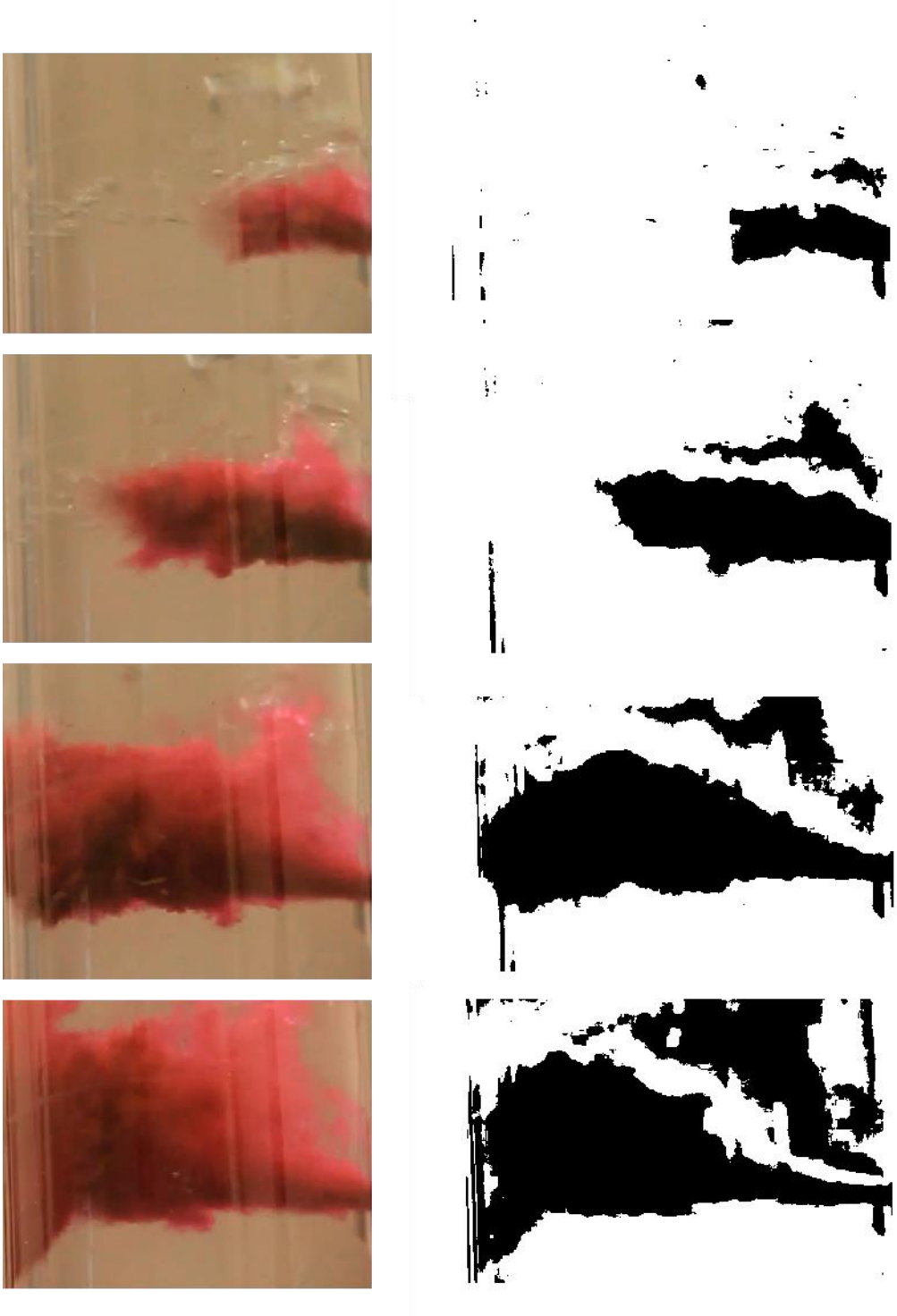

Figure 3-16 Histogram of red components in a RGB image

It can be seen from Figure 3-16 that the main characteristics of the mixing zone in the original images are captured in the binary images. Transforming the original images into binaries images as shown in Figure 3-16 allows us to analyze hundreds of frames in the videos quickly.

3.5.2. Analysis of Dye Tracer Experiment Results

The statistical results of the dye tracer experiment discussed in this chapter were obtained using the set of binary images introduced in Section 3.5.1. The first part of this section elaborates the oscillation pattern of the mixing zone in the turbulent flow when the injection rate is low, and the second part explains the relationship between the penetration distance and the injection rate.

As mentioned previously in the introduction of Section 3.5, the shape of the mixing zone was not stable with low injection rate but quite stable with high injection rate. More stable mixing zone and longer penetration distance are more favorable to us because it allows us to measure chloride concentration of the liquid from the feed zone with more flexibility without having to align the tool closely against the wall of the wellbore. As a result, we need to design our measurement strategy more carefully with low flow rate from the feed zone. The frequency at which each shape of mixing zone appeared under low injection rate is illuminated in the histogram shown in Figure 3-17.

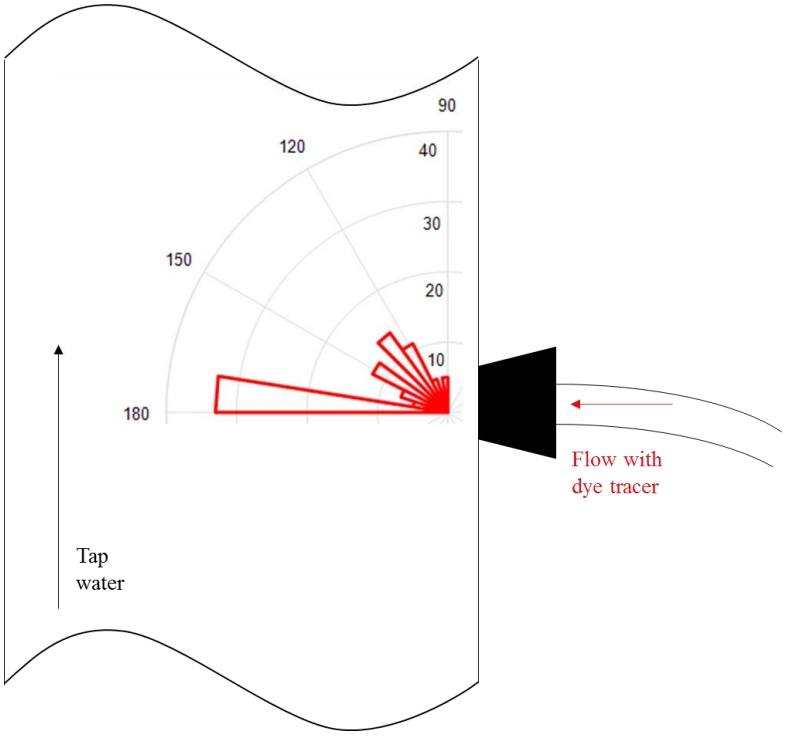

Figure 3-17 Histogram of mixing zone distribution under low injection rate

Fortunately, from Figure 3-17 we can see that the horizontal penetration, which gives the longest penetration distance, has the highest frequency. This means that the measurement locations shown in Figure 3-10 were influenced mostly by the fluid coming from the feed zone rather than the fluid below the feed zone. This observation is consistent with the trend in the violin plot shown in Figure 3-12 that the violins are wider in the upper part (high concentration) and narrower in the lower part (low concentration). In addition, this

observation also indicates that it is better to measure feed zone properties right in the cross-sectional area encompassing the inlet.

Similar analysis was done with higher injection rate, and the distributions of penetration distances under different injection rates are shown in both Figure 3-18 and Figure 3-19. The vertical axes in Figure 3-18 and Figure 3-19 indicate the percentage of well diameter penetrated by the fluid from the feed zone. When the percentage is one, the entire cross section of the well is penetrated, like shown in Figure 3-14.

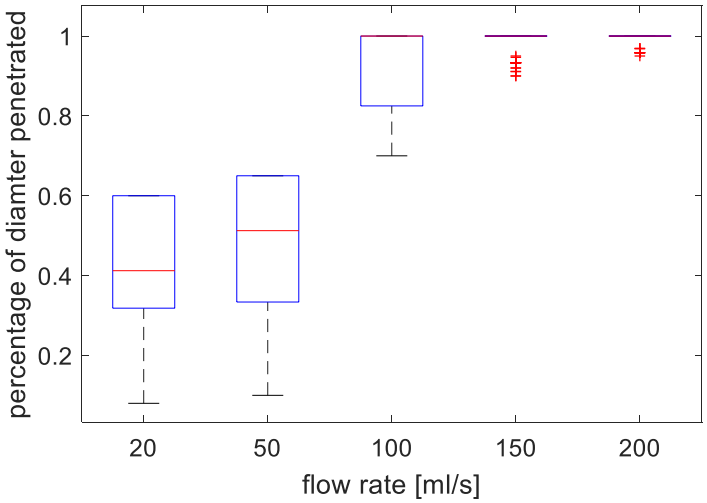

Figure 3-18 Box plot of penetration distance distribution

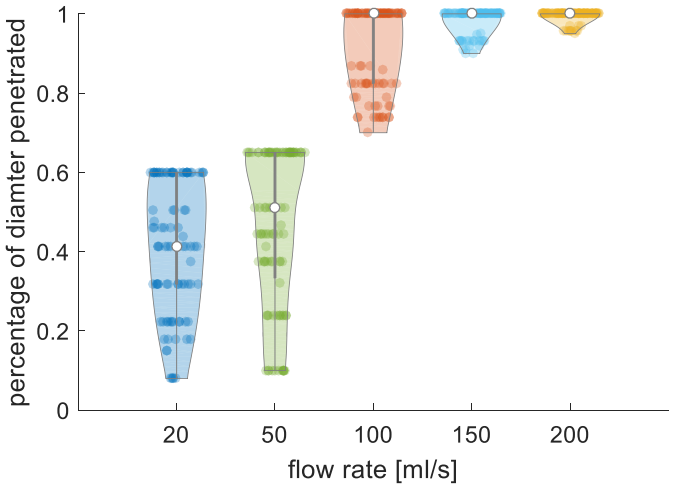

Figure 3-19 Violin plot of penetration distance distribution

It can be seen from Figure 3-18 and Figure 3-19 that the penetration distance increases with the injection rate. The boxes in Figure 3-18 and the violins in Figure 3-19 are shorter with higher injection rate, because the mixing zone is more stable with higher injection rate. With injection rate that is higher than about 80 ml/s, the entire cross section of the

wellbore could be penetrated. The shapes of the violins in Figure 3-19 are similar to those in Figure 3-12. All the violins are wider in the upper part and narrower in the lower part, which demonstrates the consistency between the experiments.

3.6. Chapter Summary

Experimental studies conducted to support the analytical model are introduced in this chapter, including calibration of the downhole tool to measure chloride concentration, test of the downhole tool in two-phase flow, measurement of chloride concentration of the liquid from the feed zone, and the dye tracer experiment that visualized the mixing zone around the inlet of the feed zone.

The following conclusions can be drawn from the series of experiments included in this chapter:

1. The calibration of the downhole tool revealed that the electrical potential difference between the Cl-ISE and the reference electrode is linearly related with the logarithm (base 10) of the chloride concentration. The calibration result is consistent with the calibration result obtained at Sandia National Laboratories. The linear relationship was applied to measure chloride concentration in later experiment.

2. The tool was tested in two-phase bubble flow with varying gas flow rate. The highest measurement accuracy was found when the tool was tested liquid flow. A trend could be observed that the measurement error increases with gas flow rate. However, the overall relative error is modest, and the relative error with high gas flow rate (6 SCFM) is less than 7%. Based on the range of relative error provided by the experiments, the relationship between the error in chloride concentration measurement and the error in enthalpy estimation was studied. A 7% relative error in chloride concentration measurement could result in an enthalpy estimation error of 4.82%.

3. A key assumption in the analytical model that chloride concentration of the liquid from the feed is measurable was examined through experiments. The results indicate that the highest measurement at the inlet can represent the chloride concentration of the liquid from the feed zone, which supports the assumption made in the analytical model. The distributions of chloride concentration at different distances from the inlet were measured and displayed in the box plots and violin plots. Measurements taken at longer distance from the inlet have larger variation, because the mixing zone is wider at locations further from the inlet.

4. In the dye tracer experiments, liquid from the feed zone was dyed with red color and videos were taken recording the mixing procedure. The videos were treated with a computer vision method, and the original images were transformed into binary images to simplify the analysis procedure. Statistical study of the videos provided distributions of different shapes of the mixing zone under varying injection rate from the feed zone port. It was found that under low injection rate, the mixing zone was not stable and oscillated with the turbulent flow. Under high injection rate, the mixing zone was stable, and the fluid from the feed zone could penetration the entire cross section of the wellbore when the injection rate was higher than about 80 ml/s. Distributions of the mixing zone indicate that even with low injection rate, the horizontal penetration has the highest frequency. This observation supported our measurement strategy that the tool was moved in horizontal direction from the inlet, as shown in Figure 3-10.

Chapter 4

4. Numerical Simulation of Two-Phase Flow in Pipes with Feed Zone Using ANSYS Fluent

In the analytical model, an assumption is made that the chloride concentration measured at the inlet of a feed zone can represent the actual chloride concentration of the liquid from the feed zone. This assumption is important for determining downhole enthalpy with multiple feed zones, because measuring the chloride concentration from the feed zone allows us to calculate the liquid flow rate from the feed zone based on chloride mass balance. In Chapter 3, experimental studies to support this assumption are illustrated, and the mixing zone was visualized through the dye tracer experiments. In this chapter, the assumption is studied by numerical methods. Conventional numerical methods to study wellbore behavior in two-phase geothermal wells often focus on simulation and prediction of well logs, including pressure log, temperature log, etc., without paying attention to the detailed fluid mechanics. The mixing process of feed zone fluid with well fluid in geothermal wells has been rarely studied. In this chapter, the flow behavior in geothermal wells is studied from a new perspective with specific focus on feed zones.

In mechanical engineering and chemical engineering, a common method to model turbulent flow is computational fluid dynamics (CFD). According to Anderson and Wendt (1995), the art of CFD is about replacing the partial differential equations governing the flow behavior with numbers and advancing these numbers spatially and temporally to achieve a numerical description of the flow field. In this case, our flow field of interest is the mixing zone at the inlet of the feed zone. Similar mixing dynamics have been studied in the literature. Yule et al. (1993) reviewed modeling and simulations of confined jet flow using CFD methods. Duer (2011) studied CFD modeling of jet flow into a circular reservoir through a sidewall inlet, which is very similar to the experiment explained in Chapter 3. Mohan et al. (2015) modeled mixing augmentation by multiple lobed jets using ANSYS Fluent, which is a commercial CFD software tool. In this work, ANSYS Fluent was used to simulate two-phase flow in vertical wells with feed zones and to visualize the mixing zone. The simulation result was compared to the experimental result, and consistency was found between the two results. Besides the jet flow, an annular inlet was considered in the model to simulate fractures crossing the wellbore.

4.1. Simulation Models

The simulation model discussed in this section means the configuration of the pipes and the flow system. It is important to design a proper model that satisfies the purpose of study before actually running the simulation. In this work, two models were designed for Fluent simulation in order to include two different types of feed zone inlets.

In the experiments discussed in Section 3.4 and Section 3.5, the feed zone inlet is an injection port. In order to compare the simulation result with the experiment result, the feed zone inlet in the first model was made similar to the injection port in the experiment. Figure 4-1 shows a schematic of the first model.

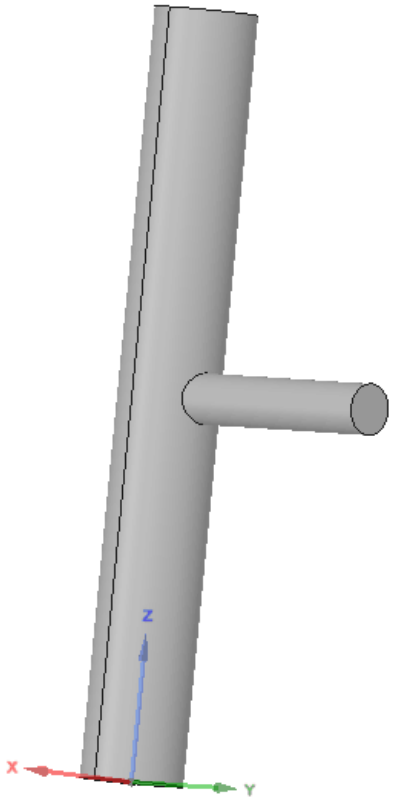

Figure 4-1 Schematic of the first simulation model

In the first model, liquid and gas flow from the bottom to the top (along the z direction in Figure 4-1), liquid and gas from the feed zone enter the wellbore from a horizontal pipe connected to the well through a sidewall port. The wellbore diameter is 0.2 m, which is close to the dimeter of the artificial well shown in Figure 3-4, and the diameter of the horizontal pipe is 10 cm.

In practice, fluid in the formation often flows into the wellbore through a fracture. However, it is difficult to create a fracture in our artificial well in the laboratory without damaging it. It is more feasible to create a fracture feed zone in the simulation model. Therefore, the second model takes into account a horizontal fracture crossing the wellbore, instead of a single injection port. The horizontal fracture is marked by the green annular area in Figure 4-2.

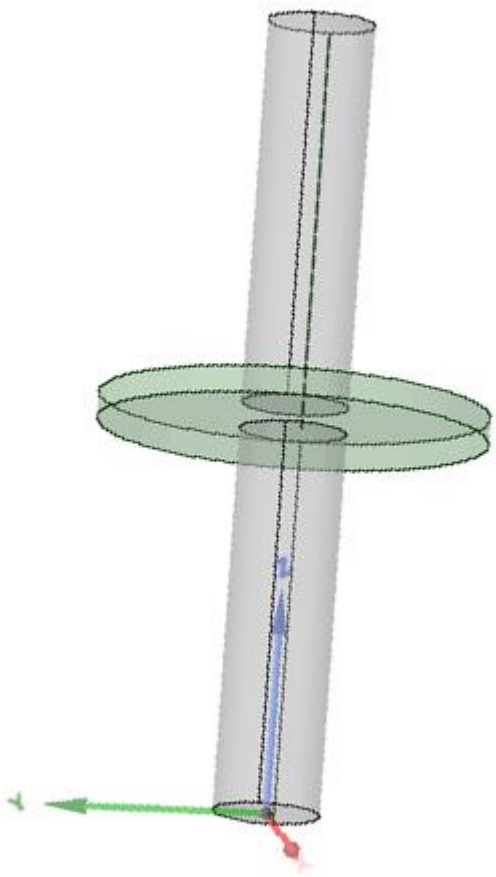

Figure 4-2 Schematic of the second simulation model

In the second model shown in Figure 4-2, liquid and gas from the feed zone enter the wellbore through the horizontal fracture uniformly from all directions on the horizontal plane marked by the green disk. Liquid and gas in the well still flow from the bottom to the top (along the z direction). The diameter of the wellbore is 0.4 m, and the aperture of the fracture was set to be 5 cm.

Boundary conditions in the two models are same. The boundary condition at the bottom of the well was set to be constant flow rate, and at the top of the well it was open boundary. The boundary condition at the feed zone inlet was also constant flow rate. The wall of the wellbore was actually no-flow boundary.

4.2. Input Variables

The input variables of the simulation include:

(1) Liquid flow rate in the well;

(2) Gas flow rate in the well;

(3) Liquid flow rate from the feed zone;

(4) Gas flow rate from the feed zone;

(5) Chloride concentration of the liquid in the well;

(6) Chloride concentration of the liquid from the feed zone;

The values of the input variables for the two models described in Section 4.1 are shown in Table 4-1

Table 4-1: Input variables for the first model and the second model

	The first model	**The second model**
Feed zone inlet type	Horizontal injection port	Horizontal fracture
Liquid flow rate in the well	35 kg/s	35 kg/s
Gas flow rate in the well	4 kg/s	4 kg/s
Liquid flow rate from the feed zone	10 kg/s	20 kg/s
Gad flow rate from the feed zone	1 kg/s	2.5 kg/s
Chloride concentration in the well	0 mol/L	0 mol/L
Chloride concentration from the feed zone	0.37 mol/L	0.1 mol/L

The chloride concentration of the liquid in the well was set to zero for two reasons. The first reason is that the liquid in the well was tap water in the experiment, and it is preferable to have same setting with the experiment so that the result from simulation and the result from experiment are comparable. The second reason is setting background chloride concentration to zero could help make the mixing zone sharper and clearer. The liquid flow rate from the feed zone was set to be larger in the second model because the cross-sectional area at the inlet is larger in the second model.

4.3. Simulation Results

After specifying the simulation model and the input variables, Fluent computed the flow field by applying the finite element method. The simulation results from the first model are shown in Figure 4-3 – Figure 4-6, and the simulation results from the second model are shown in Figure 4-7 – Figure 4-10.

The first model resembles the dye tracer experiment discussed in Section 3.5. Figure 4-3 shows the sodium chloride mass fraction in the first model. Comparing Figure 4-3 with Figure 3-13, we can find similarities between the shape of the mixing zone obtained from the experiments (shown in Figure 3-13) and the shape of the mixing zone obtained from the simulation (shown in Figure 4-3). From Figure 4-3 it can be seen that the chloride

concentration at the inlet is almost same as the chloride concentration in the feed zone, which supports the assumption made in the analytical model.

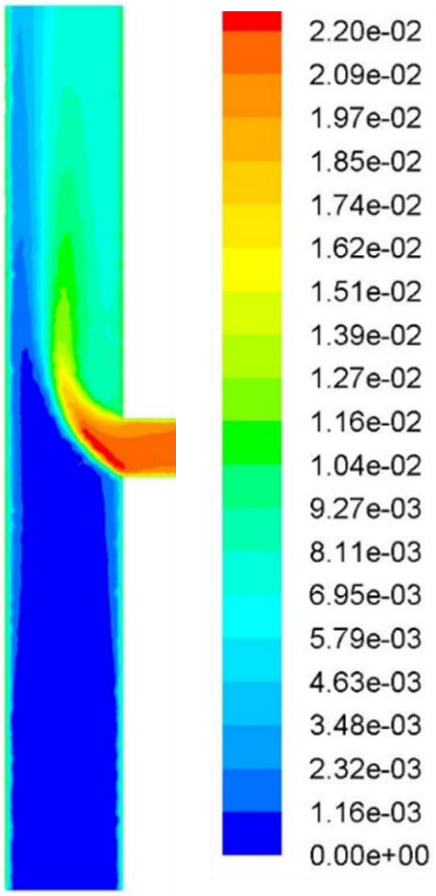

Figure 4-3 Sodium chloride mass fraction in the first model

Nevertheless, the oscillating behavior of the mixing zone observed in the experiments was not repeated in the simulation, indicating that the flow in the experiments was more turbulent than that in the simulation. Although the flow in the simulation was less turbulent, we still found some turbulent flow features in the simulation results. Figure 4-4 shows the velocity vector field in the first model. A vortex formed in the area marked by the red rectangle in Figure 4-4.

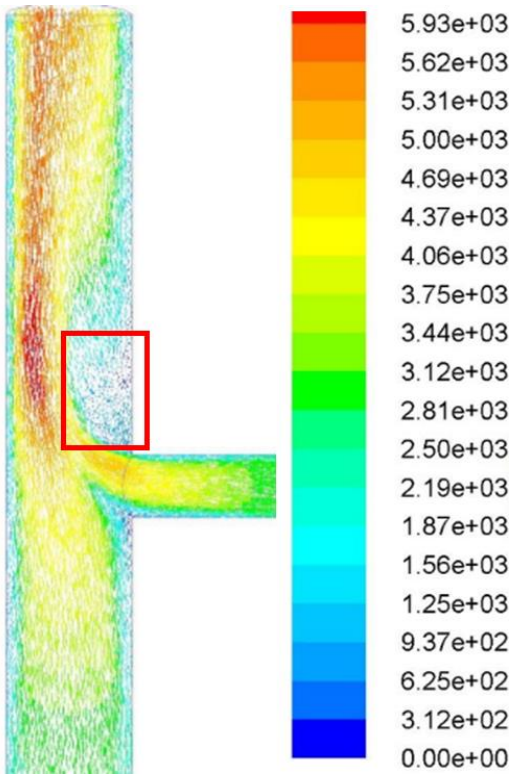

Figure 4-4 Velocity vectors colored by velocity magnitude in the first model. The unit of the color bar is mm/s

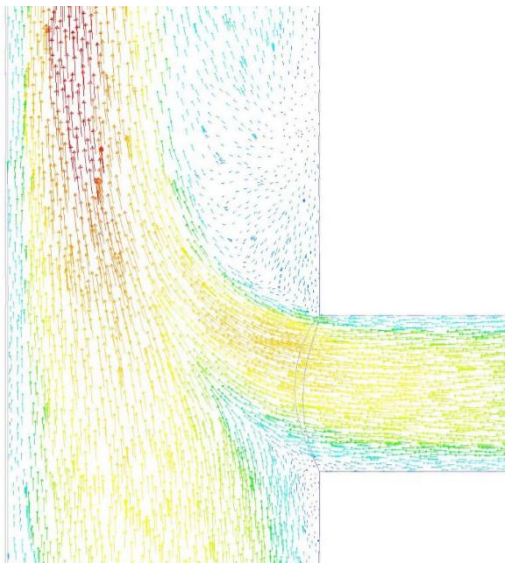

Figure 4-5 Velocity vectors in the mixing zone (zoom-in version of Figure 4-4)

Figure 4-5 is a zoom-in version of Figure 4-4. The vortex is clearer in Figure 4-5, and it can be seen that the directions of the velocity vectors are more scattered in the vortex region.

Figure 4-6 shows the volume fraction contour of the gas phase in the first model. As we can see from the color bar of Figure 4-6, the volume fraction of the gas phase is higher than 0.97 although the mass fraction of the gas phase in the well is only 0.1143. This is because the density of the gas phase equals air density in the simulation, and the air density is much smaller than liquid density. The gas phase in the experiments was also air. In the simulation, we used air instead of geothermal steam because the boiling process in the wellbore is very complicated considering change of boiling point along the wellbore due to temperature and pressure change. In the future work, simulation of the boiling fluid along the wellbore could be implemented, and current work focuses on simulation of the mixing zone at the depth of the feed zone.

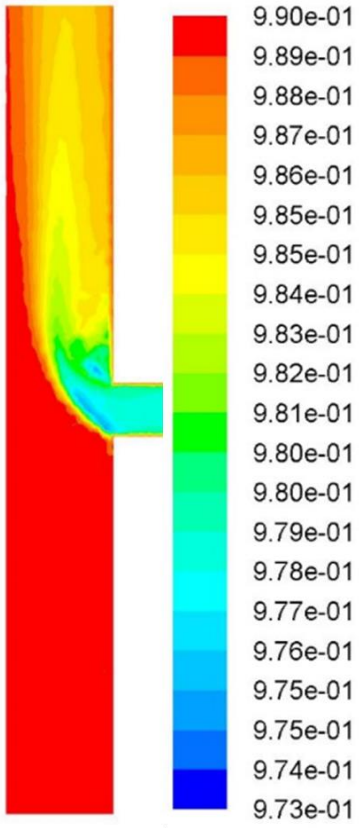

Figure 4-6 Gas volume fraction in the first model

Another observation is that the gas volume fraction contour is similar to the sodium chloride mass fraction contour. This is because the sodium chloride was actually treated as the third phase in the simulation. Dispersion of sodium chloride molecules in the liquid phase is similar to dispersion of small-diameter gas bubbles in the liquid phase.

Figure 4-7 shows the chloride mass fraction contour in the second model. Note that the two red branches in Figure 4-7 are not two inlet pipes, but are the vertical cross section of

the annular disk (i.e. the horizontal fracture) shown in Figure 4-2. Flow from the feed zone enters the wellbore uniformly from all directions on the horizontal plane.

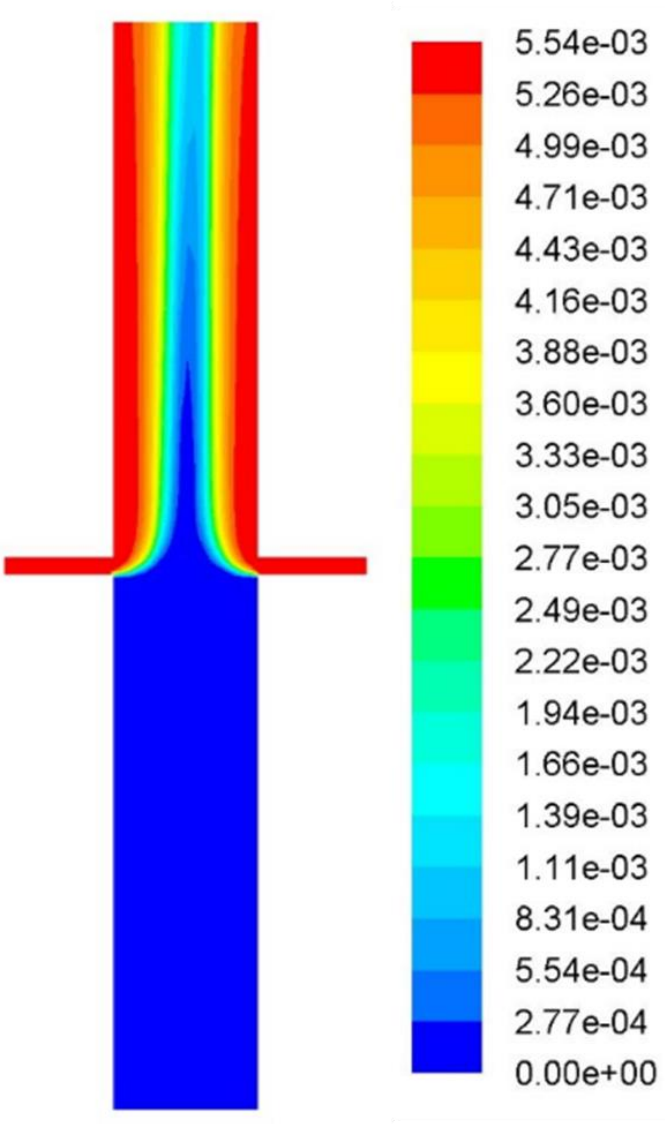

Figure 4-7 Sodium chloride mass fraction in the second model

This type of feed zone inlet is more realistic than the injection port, because it mimics the natural fracture crossing wellbore. Figure 4-8 shows the velocity vector field in the second model. As we can see from Figure 4-7 and Figure 4-8, the flow in the mixing zone in the second model is not as turbulent as that in the first model, because the cross-sectional area of the inlet is larger and flow from the feed zone is allowed to enter the wellbore from more directions in the second model.

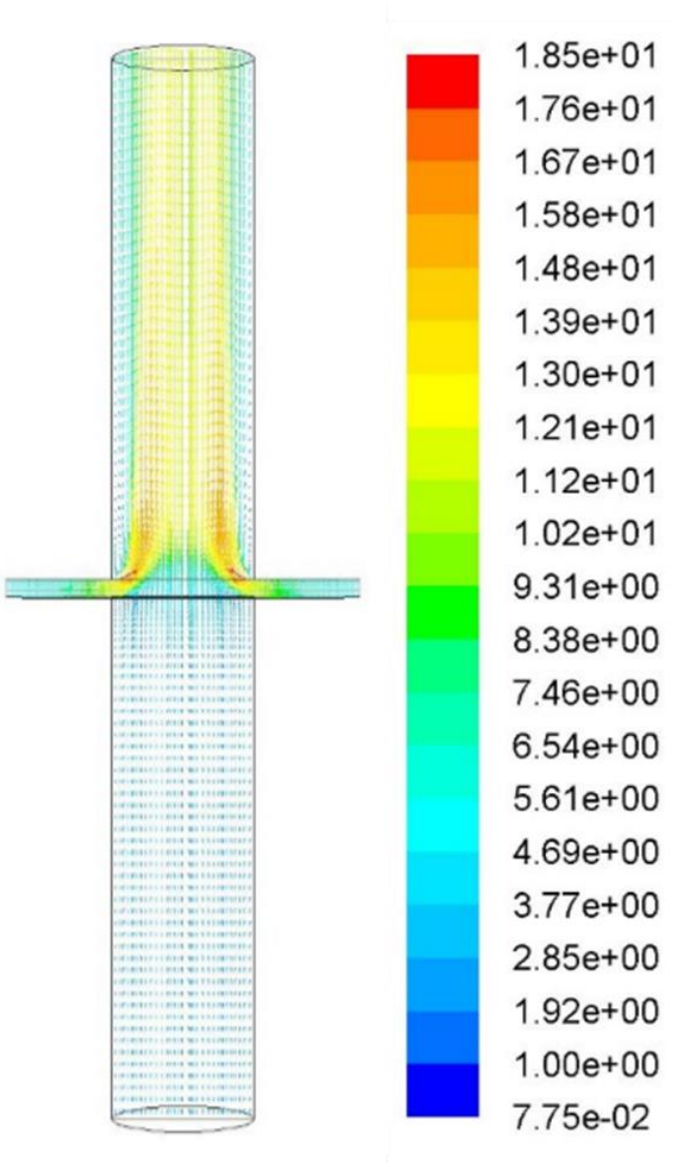

Figure 4-8 Velocity vector colored by velocity magnitude in the second model. The unit of the color bar is m/s

The unit of the color bar in Figure 4-8 is m/s. Similarly, the two branches in Figure 4-8 are not two pipes, but the vertical cross section of the horizontal fracture. In fact, the vertical cross section of the well looks the same if the well is rotated around the z axis, because of the symmetric setting of the second model.

The magnitude of velocity is smaller in Figure 4-8 than in Figure 4-4 because the wellbore diameter is larger in the second model, while liquid mass flow rate and gas flow rate in the well remain the same with those in the first model.

The second type of feed zone inlet is preferable because we have more flexibility in determining the location of the tool, because the tool could measure chloride

concentration of the liquid from the feed zone as long as it is placed anywhere against the wall of the well. Figure 4-9 shows the cross-sectional distribution of sodium chloride mass fraction at the depth of the feed zone.

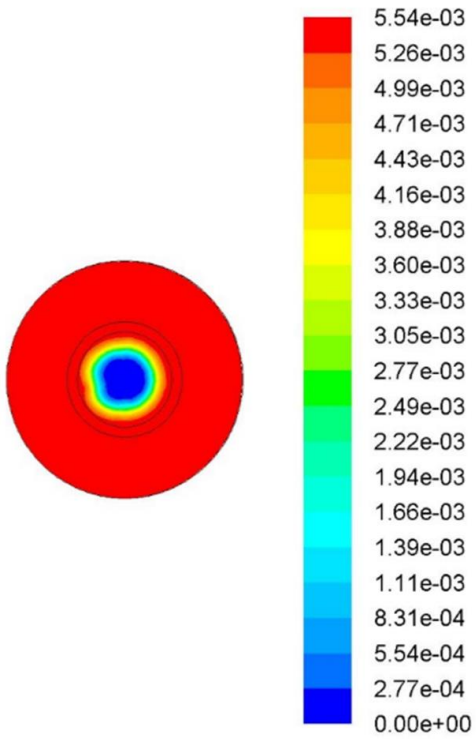

Figure 4-9 Sodium chloride mass fraction contour at the depth of feed zone

It can be seen from Figure 4-9 that an annular area in the cross section is occupied by the fluid from the feed zone. The annular area is marked by the red color (high chloride concentration) in Figure 4-9. The tool can measure feed zone chloride concentration accurately if is placed in the red annular area. The thickness of the annular area depends on the flow rate from the feed zone. Higher flow rate from the feed zone results in larger area of the red annular in Figure 4-9.

Cross-sectional contours of sodium chloride mass fraction changes with depth, and the shapes of the red annular area in Figure 4-9 are different at different depth due to mixing of the flow long the wellbore and uneven friction distribution. Figure 4-10 shows the contour of sodium chloride mass fraction at the top of well. The annular shown in Figure 4-9 becomes out of shape in Figure 4-10, indicating that the flow in the second model is not laminar flow, even though it is not as turbulent as that in the first model. The mixing of the fluid from the feed zone with the fluid in the well significantly influences the distribution of chloride concentration.

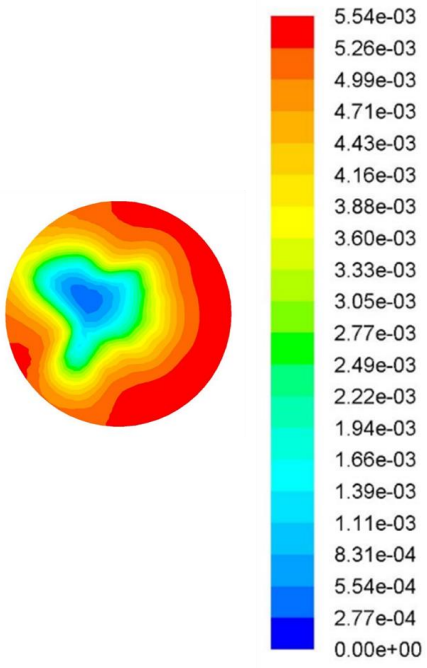

Figure 4-10 Sodium chloride mass fraction contour at the top of the well

4.4. Chapter Summary

In this chapter, numerical simulations of two-phase flow in vertical wells with feed zones are discussed. The CFD method was implemented using the software ANSYS Fluent. Two simulation models were established, considering two different types of feed zone inlet. The first model mimics the experiments illustrated in Section 3.5, and the second model mimics a horizontal fracture with an aperture of 5 cm. The following conclusions can be reached based on the simulation results:

(1) The simulation results in the first model resemble the results from the dye tracer experiment. Visualizations achieved by the simulation method and by the experimental method show a similar shape of the mixing zone. It is demonstrated both in the simulation and in the experiments that the chloride concentration of the liquid from the feed zone is measurable at the inlet of the feed zone.

(2) The velocity vector field in the first model displays turbulent features of the flow in the mixing zone, which is consistent with the experimental observation of the flow type.

(3) The second type of feed zone inlet is more realistic. The mixing zone with the second type of feed zone inlet is difficult to be visualized by experimental methods under laboratory conditions. Therefore, it was only visualized by simulation method in this chapter. A mixing zone with an annular shape was observed in the simulation results.

(4) Flow in the second model is less turbulent than that in the first model and in the experiment, but chloride concentration distribution is stilled influenced by the mixing of fluid from the feed zone with the fluid in the well.

(5) The second type of feed zone inlet is preferable because it makes measurement of chloride concentration at the inlet much easier. The tool is able to measure chloride concentration of the liquid from the feed zone accurately as long as it is placed with the annular zone shown in Figure 4-9.

Chapter 5

5. Conclusions and Future Work

5.1. Conclusions

The main objective of this work was to estimate enthalpy of the geothermal fluid downhole by measuring chloride concentration using a real-time downhole tool. The analytical model that relates the flowing enthalpy of two-phase geothermal fluid with the chloride concentration in the liquid phase was established and examined through experimental studies and simulation studies. Both experimental results and simulation results support the analytical model.

In Chapter 2, the analytical model is elaborated in different scenarios. With single feed zone, the analytical model for calculating downhole enthalpy based on chloride concentration involves chloride mass balance and total mass balance of gas and liquid. In the case of multiple feed zones, three different cases are illustrated. In Case 1 and Case 2, both the flowing enthalpy of the fluid from the feed zone and the flow enthalpy of the fluid below the feed zone can be calculated using the analytical model. In Case 3, the analytical model is modified to incorporate energy balance with mass balance. The steam enthalpy and the liquid enthalpy from the feed zone can be obtained from temperature measurement, and energy balance is applied to calculate the steam flow rate and the flowing enthalpy below the feed zone.

In the analytical model, in order to calculate liquid flow rate from the feed zone based on chloride concentration measurement, an assumption has to be made that the chloride concentration of the liquid from the feed zone is measurable at the inlet of the feed zone. This assumption is the most important assumption in the analytical model and provides basis for enthalpy calculation in the case of multiple feed zones. Therefore, this assumption was studied further and examined through experiments and simulations. The experiments and simulations are illustrated in Chapter 3 and Chapter 4 respectively.

Chapter 3 includes explanation of all the experimental work. The purpose of conducting the experiment was to test the ability of the downhole tool to measure chloride concentration in two-phase flow and to examine the feasibility of measuring chloride concentration at the inlet of the feed zone. In the experiments, the tool was first calibrated and a linear relationship was found between the voltage measured using the electrodes of the tool and the logarithm (base 10) of chloride concentration. The downhole tool was tested in an artificial well that could flow two-phase flow, and the experiment results indicate that the tool can measure chloride concentration in two-phase flow with satisfactory accuracy. Based on the range of relative error provided by the experiment, the relationship between error in chloride concentration measurement and error in enthalpy estimation was studied. It was found that when relative error in chloride concentration measurement increased from 0.01 to 0.07, the relative error in enthalpy estimation increased from 0.008 to 0.048. Chloride concentration of the liquid from the feed zone was measured by the tool at the inlet of the feed zone in the experiment. The results indicate that the highest measurement at the inlet can represent the true chloride concentration of the liquid from the feed zone, which supports the assumption made in the analytical model. The distribution of chloride concentration at different distances from the inlet were measured and displayed in the box plots and violin plots. Measurements taken at longer distance from the inlet have larger variation, because the mixing zone is wider at locations further from the inlet. In the dye tracer experiments, liquid from the feed zone was dyed with red color and videos were taken recording the mixing procedure. The videos were treated with a computer vision method, and the original images were transformed into binary images to simplify the analysis procedure. It was found that under low injection

rate, the mixing zone was not stable and oscillated with the turbulent flow. Under high injection rate, the mixing zone was stable, and the fluid from the feed zone could penetration the entire cross section of the wellbore when the injection rate was higher than about 80 ml/s.

Chapter 4 describes numerical simulations of two-phase flow in vertical wells with feed zones using ANSYS Fluent. Two types of feed zone inlet were considered in the simulation models. The first type of inlet is an injection port similar to that in the experiment, and the second type of inlet is a horizontal fracture with an aperture of 5 cm. The mixing zone from both types of inlets were visualized. The visualization obtained using the first type of inlet was compared to the dye tracer experiment, and consistency was found between the two results. The mixing zone from the second type of inlet is in annular shape.

In conclusion, the results demonstrate a successful downhole technique for measuring enthalpy in geothermal wells.

5.2. Future Work

Future work will focus on following aspects:

(1) Experimental study of the performance of the tool in more flow patterns is necessary. Currently the tool has been tested in bubble flows. Testing the tool in other flow patterns, including annular flow, slug flow and churn flow, could provide a more complete evaluation of the performance of the tool.

(2) Development of the tool to achieve higher resolution could help improve the efficiency in chloride concentration measurement.

(3) More study on measurement of the feed zone temperature is necessary.

(4) It is useful to conduct experiments with the tool in real geothermal wells in field application.

(5) The simulation model could be improved by considering the boiling process in the wellbore. Change of boiling point with pressure and temperature should be incorporated into the simulation model.

Nomenclature

Cl = chloride concentration on a volumetric base

q_l = volumetric flow rate of the liquid phase

$\dot{m}_{cl}$ = mass flow rate of chloride

$Cl_{surface}$ = chloride concentration at the surface

$Cl_{downhole}$ = is chloride concentration in the downhole

$q_{lsurface}$ = volumetric flow rate of the liquid phase at the surface

$q_{ldownhole}$ = volumetric flow rate of the liquid phase in the downholw

$\dot{m}$ = total mass flow rate

ρ_l = density of liquid phase

x = steam fraction

h_t = total enthalpy

h_l = enthalpy of liquid water

h_s = enthalpy of steam

q_{lin} = volumetric flow rate of the liquid phase from the feed zone

Cl_{in} = chloride concentration of the liquid from the feed zone

Cl_{below} = chloride concentration of the liquid below the feed zone

Cl_{above} = chloride concentration of the liquid above the feed zone

q_{lbelow} = volumetric flow rate of the liquid phase below the feed zone

$\dot{m}_{below}$ = total mass flow rate of steam and water below the feed zone

ρ_{lin} = density of the liquid from the feed zone

ρ_{lbelow} = density of the liquid below the feed zone

m_{lbelow} = liquid mass flow rate below the feed zone

m_{sbelow} = steam mass flow rate below the feed zone

m_{lin} = liquid mass flow rate from the feed zone

$m_{\sin}$ = steam mass flow rate from the feed zone

m_{labove} = liquid mass flow rate above the feed zone

m_{sabove} = steam mass flow rate above the feed zone

Cl-ISE = chloride-ion selective electrode

M = chloride concentration in mol/L

Voltage = difference in electrical potential between the chloride-ion selective electrode and the reference electrode

SCFM = standard cubic feet per minute

$\varepsilon_{enthalpy}$ = relative error in enthalpy estimation

$\varepsilon_{chloride}$ = relative error in chloride concentration measurement

RGB = Red, Green and Blue

CFD = computational fluid dynamics

References

Anderson, J.D. and Wendt, J., 1995, "Computational Fluid Dynamics", McGraw-Hill, New York.

Atalay, N., 2008, "Downhole Enthalpy Measurement in Geothermal Wells with Fiber Optics", Stanford Geothermal Program Report SGP-TR-186.

Brennen, C.E., 2005, "Fundamentals of Multiphase Flow", Cambridge University Press.

Cieslewski, G., Hess, R. F., Boyle, T. J., Yelton, W. G., 2016, "Development of a Wireline Tool Containing an Electrochemical Sensor for Real-time pH and Tracer Concentration Measurement", Geothermal Resources Council, Davis, California, CA.

Corbin, W. C., Cieslewski G., Hess R. F., Klamm B. E., Goldfarb L., Boyle T. J., and Yelton W. G., 2017, "Development of a Downhole Tool for Measuring Enthalpy in Geothermal Reservoirs", Proceedings of the 42th Workshop on Geothermal Reservoir Engineering.

Duer, M., 2011. "Passive Mixing Systems Improve Storage Tank Water Quality (PDF)", Opflow, 37(8), pp.20-23.

Gendenjamts, O.E., 2003, "Interpretation of Chemical Composition of Geothermal Fluids from Árskógsströnd, Dalvík, and Hrísey, N-Iceland and in the Khangai Area, Mongolia", The United Nations University, Geothermal Training Programme, Iceland, Report 10, 219 – 252.

Grant, M.A., 1982, "Geothermal reservoir engineering", John Wiley & Sons, Ltd.

Hess, R. F., Cieslewski, G., Boyle, T. J., Limmer, S., Yelton, W. G., Bingham, S., Stillman, G., 2015, "Measuring Real-time Concentration of Ionic Tracers and pH in Geothermal Reservoirs Using a Ruggedized Downhole Tool", Proceedings of the 40th Workshop on Geothermal Reservoir Engineering, SGP-TR-204.

Hirtz, P., Lovekin, J., Copp, J., Buck C. and Adams M., 1993, "Enthalpy and Mass Flowrate Measurement for Two-Phase Geothermal Production by Tracer Dilution Techniques", 18th Workshop on Geothermal Reservoir Engineering, SGP-TR-145.

Hirtz, P. and Lovekin, J., 1995, "Tracer Dilution Measurements for Two-phase Geothermal Production: Comparative Testing and Operating Experience", Geothermal Resources Council, Davis, CA, No. CONF-951037--.

Hyndman, R.D., Davis, E.E. and Wright, J.A., 1979, "The Measurement of Marine Geothermal Heat Flow by a Multipenetration Probe with Digital Acoustic Telemetry and Insitu Thermal Conductivity", Marine Geophysical Research, 4(2), pp.181-205.

Juliusson, E., 2006, "An Investigation Of Void Fraction And Dispersed-phase Velocity Measurement Techniques", Stanford Geothermal Program Report SGP-TR-181.

Juliusson, E. and Horne, R. N., 2006, "Downhole Enthalpy Measurement in Geothermal", Proceedings of 31st Workshop on Geothermal Reservoir Engineering, SGP-TR-179.

Khasani, I., Harijoko, A., Dwikorianto, T. and Patangke, S., 2010, "Development of Measurement Method of Steam-Water Two-Phase Flow System Using Single Frequency Waves", Proceedings of 35th Workshop on Geothermal Reservoir Engineering, SGP-TR-188. 2010.

Kumar, M., Horne, R.N., 1995, "Ultrasonic Rate Measurements in Two-Phase Bubble Flow", SPE 30596, presented at the 70th Annual Technical Conference & Exhibition, Dallas, TX, October 22-25.

Lovelock, B. G., 2001, "Steam Flow Measurement Using Alcohol Tracers", Geothermics, 30(6), pp.641-654.

Marini, L. and Cioni, R., 1985, "A Chloride Method for the Determination of the Enthalpy of Steam/Water Mixtures Discharged from Geothermal Wells." Geothermics, 14(1), pp.29-34.

Mohan, N.D., Prakash, K.R. and Panchapakesan, N.R., 2015. "Mixing Augmentation by Multiple Lobed Jets", American Journal of Fluid Dynamics, 5(2), pp.55-64.

Moody, F.J., 1965, "Maximum Flow Rate of a Single Component, Two-phase Mixture", Journal of Heat Transfer, 87(1), pp.134-141.

Nicholson, K., 2012, "Geothermal Fluids: Chemistry and Exploration Techniques". Springer Science & Business Media.

Yule, A.J., Damou, M. and Kostopoulos, D., 1993. "Modeling Confined Jet Flow", International Journal of Heat and Fluid Flow, 14(1), pp.10-17.